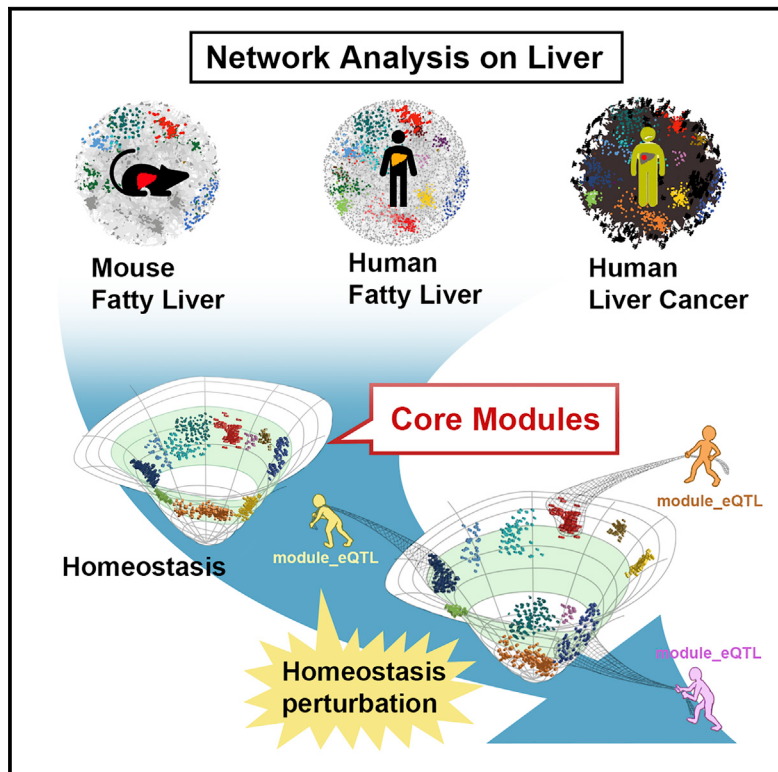


## Core liver homeostatic co-expression networks are preserved but respond to perturbations in an organism- and disease-specific manner

### Graphical abstract



### Authors

Saeed Esmaili, Peter Langfelder, T. Grant Belgard, ..., Henning Grønbæk, Christopher Liddle, Jacob George

### Correspondence

jacob.george@sydney.edu.au

### In brief

Esmaili et al. identified a core homeostatic network that is preserved between liver diseases and between species. The behavior of these networks is disease specific, while genetic variants that regulate core networks are predictive of patient survival. This study provides a road map to design core network-oriented pre-clinical studies. This ensures translatability of findings from pre-clinical models to humans and can help implement network medicine-based treatments.

### Highlights

- Liver core homeostatic networks are preserved between disease models and species
- The extent of perturbation in some of these networks predicts cancer survival
- Environmental and genetic factors impact perturbations in the core modules
- Adding non-core networks provides a nuanced model for homeostatic perturbations



Article

# Core liver homeostatic co-expression networks are preserved but respond to perturbations in an organism- and disease-specific manner

Saeed Esmaili,<sup>1,2</sup> Peter Langfelder,<sup>3</sup> T. Grant Belgard,<sup>4</sup> Daniele Vitale,<sup>1</sup> Mahmoud Karimi Azardaryany,<sup>1</sup> Ghazal Alipour Talesh,<sup>1</sup> Mehdi Ramezani-Moghadam,<sup>1</sup> Vikki Ho,<sup>1</sup> Daniel Dvorkin,<sup>4</sup> Suat Dervish,<sup>5</sup> Brian S. Gloss,<sup>5</sup> Henning Grønbæk,<sup>6</sup> Christopher Liddle,<sup>1</sup> and Jacob George<sup>1,7,\*</sup>

<sup>1</sup>Storr Liver Centre, Westmead Institute for Medical Research, Westmead Hospital and University of Sydney, Sydney, NSW, Australia

<sup>2</sup>Liver and Pancreatobiliary Diseases Research Center, Digestive Disease Research Institute, Shariati Hospital, Tehran University of Medical Sciences, Tehran, Iran

<sup>3</sup>The Jane and Terry Semel Institute for Neuroscience and Human Behavior, David Geffen School of Medicine, University of California, Los Angeles, Los Angeles, USA

<sup>4</sup>The Bioinformatics CRO, Niceville, FL, USA

<sup>5</sup>Westmead Research Hub, Westmead Institute for Medical Research, Sydney, NSW, Australia

<sup>6</sup>Department of Hepatology and Gastroenterology, Aarhus University Hospital, Aarhus, Denmark

<sup>7</sup>Lead contact

\*Correspondence: jacob.george@sydney.edu.au

<https://doi.org/10.1016/j.cels.2021.04.004>

## SUMMARY

Findings about chronic complex diseases are difficult to extrapolate from animal models to humans. We reason that organs may have core network modules that are preserved between species and are predictably altered when homeostasis is disrupted. To test this idea, we perturbed hepatic homeostasis in mice by dietary challenge and compared the liver transcriptome with that in human fatty liver disease and liver cancer. Co-expression module preservation analysis pointed to alterations in immune responses and metabolism (core modules) in both human and mouse datasets. The extent of derailment in core modules was predictive of survival in the cancer genome atlas (TCGA) liver cancer dataset. We identified module eigengene quantitative trait loci (module-eQTL) for these predictive co-expression modules, targeting of which may resolve homeostatic perturbations and improve patient outcomes. The framework presented can be used to understand homeostasis at systems levels in pre-clinical models and in humans. A record of this paper's transparent peer review process is included in the supplemental information.

## INTRODUCTION

Hepatocellular cancer (HCC) is the second most common cause of cancer-related death globally (Ferlay et al., 2015). Hepatitis viruses such as hepatitis B and C are the major etiological agents, but recent increases in cancer incidence are partly attributed to the dramatic escalation in the prevalence of metabolic (dysfunction) associated fatty liver disease (MAFLD) that affects a quarter of the global population (Eslam et al., 2020; Younes and Bugianesi, 2018; Younossi et al., 2018, 2015). Steatohepatitis, the inflammatory form, and to a lesser extent hepatic steatosis are established risk factors for both cirrhosis and HCC (Alexander et al., 2019). The development of cirrhosis contributes to the progression to HCC (Marengo et al., 2016); however, cancer can also develop in non-cirrhotic patients with MAFLD (Hardy et al., 2016).

A recent analysis demonstrated that cells with oncogenic mutations are present even in normal tissues including the liver (Yizhak et al., 2019). Thus, the occurrence of mutations per se

does not explain cancer development, and it has been suggested that alterations in the tissue microenvironment are pivotal to select for cells that form tumors (DeGregori, 2017). Thus, the outcome of cancers can be thought of as both cancer cell and microenvironment dependent, including of the local immune response. Investigating how disturbances in hepatic homeostasis leads to an increased risk of HCC is critical to design effective prevention and treatment strategies. This requires developing tissue and context specific knowledge on homeostatic mechanisms.

Homeostatic states have a dynamic range which means that they can tolerate some degree of fluctuation; environmental and genetic factors impact this range (Hu et al., 2016; Nijhout et al., 2017). Here, we used mice exposed to different combinations of macro- and micronutrients to perturb liver homeostasis. The mice developed a spectrum of liver pathologies to which we applied a systems approach with network analysis on genome-wide transcriptomes; similar analyses were undertaken in healthy and diseased human liver (MAFLD) and in liver cancer



datasets. Subsequently, we investigated the preservation of gene co-expression modules between datasets to find “core modules” for homeostasis. Interestingly, co-expression modules related to the immune response and metabolism were consistently preserved between species. However, the direction of changes in these modules was indicative of organism- and disease-specific responses. We hypothesized that the degree of perturbation of core modules is relevant to patient outcomes. Indeed, expression levels of some components of the core modules were predictive of patient survival. Finally, we looked for genetic variants related to the expression levels of modules predictive of survival and found module regulators (module-eQTLs) as potential therapeutic targets for liver cancer.

## RESULTS

### Dietary interventions perturb hepatic homeostasis in mice

We hypothesized that the mechanisms that maintain hepatic homeostasis in mice and humans are largely preserved. To explore this, we challenged mice with diets that differed in macro- and micronutrients and studied liver pathology and transcriptomes at systems level. Subsequently, we used the insights gained to explain homeostatic perturbations in clinical fatty liver and in liver cancer (Figures 1A and 1B). The initial study was conducted with well-established dietary models containing different combinations of sucrose and cholesterol with and without cholic acid (CA) for 8 weeks (Figure 1A). No differences were observed in liver weight and liver-to-body weight ratio in mice fed a diet high in sucrose (HS) or a combination of sucrose and cholesterol (HS\_Chol2%) (Figures S1A–S1C). However, liver weight and liver-to-body weight ratio increased in the diets that contained CA: HS\_Chol2%\_CA, Chol2%\_CA, and CA (Figures S1A–S1C).

Hematoxylin and eosin (H&E) staining indicated the presence of marked hepatic inflammation in diets that contained both CA and cholesterol: HS\_Chol2%\_CA and Chol2%\_CA (Figure 1A). Inflammation was also observed in the HS\_Chol2%-diet-fed mice; however, diets containing just sucrose or CA did not induce inflammation. Consistently, flow cytometry analysis on liver of mice confirmed an increase in the population of myeloid and lymphoid cells by the HS\_Chol2%-CA and Chol2%-CA diets (Figures S1D–S1G). Principal component and supervised partial least squares discriminant analysis plots based on marker median mean fluorescence intensity (MFI) show a clear separation of HS\_Chol2%\_CA and Chol2%\_CA diets from the rest (Figures S1H and S1I).

We also fed mice diets with lower concentrations of cholesterol (0.2%) and sucrose, with and without CA. The liver of HS\_Chol0.2%-fed mice did not demonstrate liver pathology at 8 or 16 weeks (extended data on Mendeley: <https://doi.org/10.17632/sfng2h249n.1>) consistent with reports that higher concentrations of cholesterol are required to induce liver inflammation in mice (Friedman et al., 2018). However, when combined with CA (HS\_Chol0.2%\_CA) the mice showed severe liver inflammation similar to that seen with the HS\_Chol2%\_CA diet at 8 weeks (extended data on Mendeley: <https://doi.org/10.17632/sfng2h249n.1>). This indicates that diets containing both cholesterol and CA perturb hepatic homeostasis.

### Weighted gene co-expression network analysis shows alterations in immune responses and in metabolism by cholesterol and cholic acid

To explore alterations in the landscape of liver homeostatic responses to diet in an unbiased manner, we performed RNA sequencing of liver from mice fed the 6 diets. Differential gene expression analyses showed thousands of differentially expressed (DE) genes at a false discovery rate (FDR) <0.05. In most of the diet contrasts (Figure 2A), HS\_Chol2%\_CA- and Chol2%\_CA-fed mice showed the largest number of DE genes compared with normal chow, while HS-diet-fed mice had the lowest number. The PCA plot after pre-processing shows relatively clean separation of samples by diet, suggesting that diet has a strong, readily observable effect on RNA expression (Figure 2B).

We reasoned that a co-expression network analysis (WGCNA) (Zhang and Horvath, 2005) would allow us to define transcriptional modules enabling a study of the effect of each diet on the co-expression modules. This approach reduces thousands of genes to a small number of transcriptionally coherent modules that represent distinct transcriptional responses to diet. We used two different module identification settings to produce two sets of module labels—one resulting in larger, more robust co-expression modules (called “main” modules) and a second that produces a finer split of those main modules that can be thought of as consisting of 2 or more submodules (Figure 2C).

Since each co-expression module groups together correlated genes, each module can be represented by a single representative expression profile called a module eigengene (ME). After module identification we analyzed the enrichment of genes in each co-expression module and the association of MEs with diet (Figure 2D). Of the 15 co-expression modules, 9 were associated with diet based on the overall F test FDR < 0.05. Of note, a majority of the modules enriched for immune and metabolic pathways. Analysis of ME association with diet indicated that mouse (m) M1.1 (enriched for immune system processes) is upregulated in the HS\_Chol2%\_CA and Chol2%\_CA diets (Figures 2D and 2E). However, mM2 that is enriched in metabolic pathways shows the opposite behavior to mM1.1 and is downregulated by these diets (Figure 2F). These two modules were highly but negatively correlated ( $\text{cor} = -0.91$ ,  $p = 4.3\text{e}-09$ , Figure 2G). It should be noted that mM3.1 is also enriched in metabolic pathways and is downregulated in HS\_Chol2%\_CA, Chol2%\_CA, and CA diets (Figure 2H). mM3.1 shows a negative correlation with mM1.1 ( $\text{cor} = -0.86$ ,  $p = 2.9\text{e}-07$ ) and a positive correlation with mM2 ( $\text{cor} = 0.66$ ,  $p = 0.00083$ ) (Figure 2I).

Module eigengenes lead to a natural measure of similarity (membership) of all individual genes to all modules. This can be measured by kME, which is the correlation of the expression of the gene to the module eigengene. Genes with highest kME, called hub genes, are centrally located inside the module and represent the expression profile of the entire module. Expression of module eigengenes across the 6 diets for the mM1.1, mM2, and mM3.1 and top hub genes related to mM1.1 (*Sema4d*, *Clec7a*, *Arhgap25*, *Sirpa*, etc.), mM2 (*Sod1*, *Ndufs1*, *Grep1*, *Uqcrc2*, etc.) and mM3.1 (*Nit2*, *Tst*, *Serpina1d*, *Gm13775*, etc.) are shown in Figures 2E, 2F, and 2H and are available in Document S1.

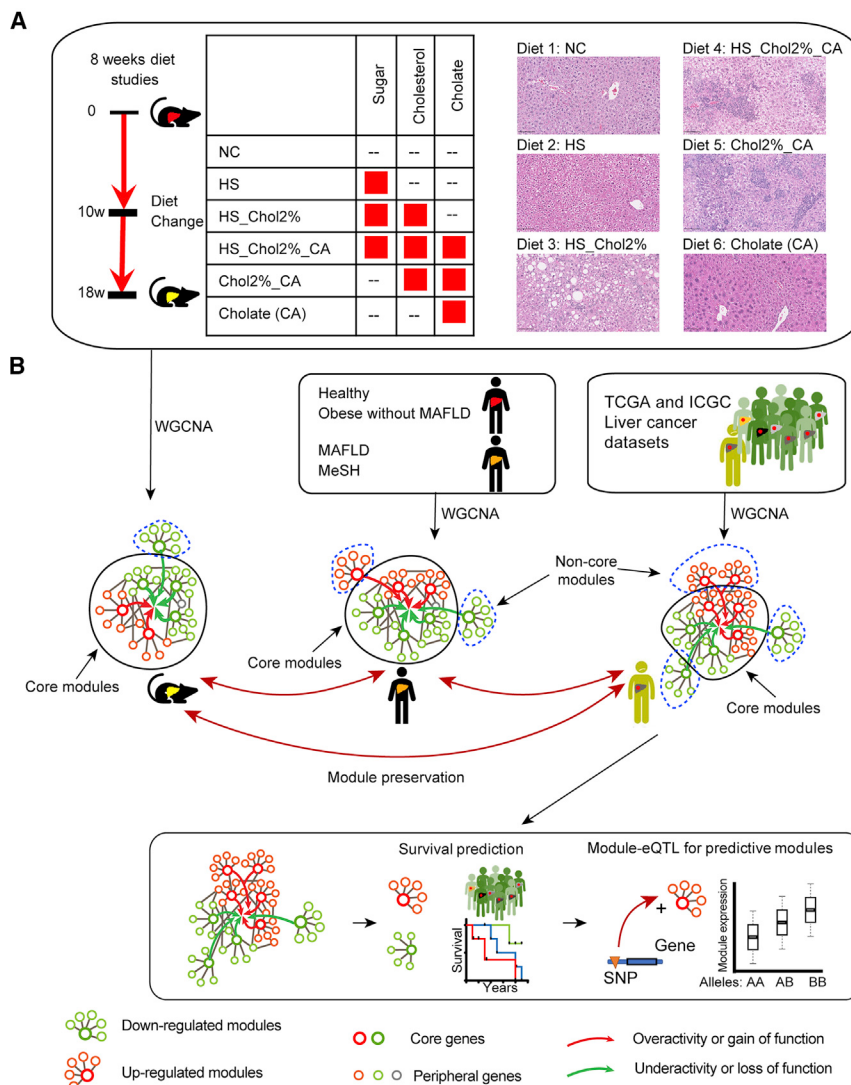


**Figure 1. A framework workflow on mouse models, human fatty liver, TCGA, and ICGC liver cancer datasets to define homeostatic perturbations and find therapeutic targets**

(A) To perturb the liver homeostatic state, mice were challenged with dietary interventions for 8 weeks ( $n = 8$  mice per group). H&E staining of mice liver demonstrates liver steatosis and mild inflammation in diet 3 (HS-Chol2%) and severe inflammation in diet 4 (HS\_Chol2%\_CA) and diet 5 (Chol2%\_CA). (Magnification = 20 $\times$ ; scale bar, 100  $\mu$ m)

(B) Schematic presentation of the framework with WGCNA and preservation analysis on mice dietary models, human metabolic (dysfunction)-associated fatty liver disease (MAFLD), and liver cancer. We defined core homeostatic perturbation networks as modules that are preserved between mice and human datasets. The up- and down-regulation (behavior) of modules are presented as red and green colors, respectively. Behavior of some of the modules were predictive of liver cancer outcome. We found module-eQTLs for modules that were predictive of survival. Module-eQTLs can regulate the behavior of a module, hence, are potential therapeutic candidates. See also Figure S1.

NC, normal chow; HS, high sucrose; HS\_Chol2%, high sucrose + high cholesterol (2%); HS\_Chol2%\_CA, high sucrose + high cholesterol (2%) + cholic acid; Chol2%\_CA, high cholesterol (2%) + CA; CA, cholic acid;

In sum, our analysis shows that the liver of mice on diets containing cholesterol and CA demonstrate greater homeostatic disturbances, with immune response modules being up-regulated and metabolism modules being downregulated. A schematic of homeostasis and perturbed homeostasis as the result of dietary influences is depicted in Figure 2J.

#### Validation of weighted gene co-expression network analysis co-expression modules in STRING and BioGRID datasets and module recovery by other network analysis methods

To explore whether mouse co-expression modules contain the information related to validated networks, we carried out enrichment analysis of the mouse modules in protein-protein interactions (PPI) networks from the BioGRID and STRING databases. The STRING database contains confidence scores that can be used to filter the network to contain only the most confident interactions. The results are shown in Table S1. We find that many though not all

of our modules are strongly enriched in both the BioGRID and STRING PPI networks. Modules mM1.1, mM2, mM3.1, and a module related to angiogenesis (mM7) are strongly enriched in both databases at all thresholds except mM7 at the highest threshold. These modules are the most biologically informative modules in our weighted gene co-expression network analysis (WGCNA) and will be discussed later.

In addition, we performed network analysis of mouse liver data using 5 different network construction methods. We used the R package MODA which can use 3 different clustering methods as well as 2 mutual information-based relevance network methods. Specifically, we used the hierarchical clustering-based MODA analysis, Louvain clustering (also implemented in MODA), spectral clustering (MODA), and relevance networks based on measures of mutual information, namely ARACNE (Margolin et al., 2006) and MRNET (Meyer et al., 2007) implemented in the R package minet (Meyer et al., 2008). Where applicable, we attempted to approximate the module identification parameters used in our WGCNA (e.g., MODA allows one to specify the soft-thresholding power, and we used the same value 8 as used in our WGCNA). We used hierarchical clustering and Dynamic Tree Cut to identify modules in the ARACNE and MRNET networks, which resulted in a large number of modules (more than 200); we merged modules

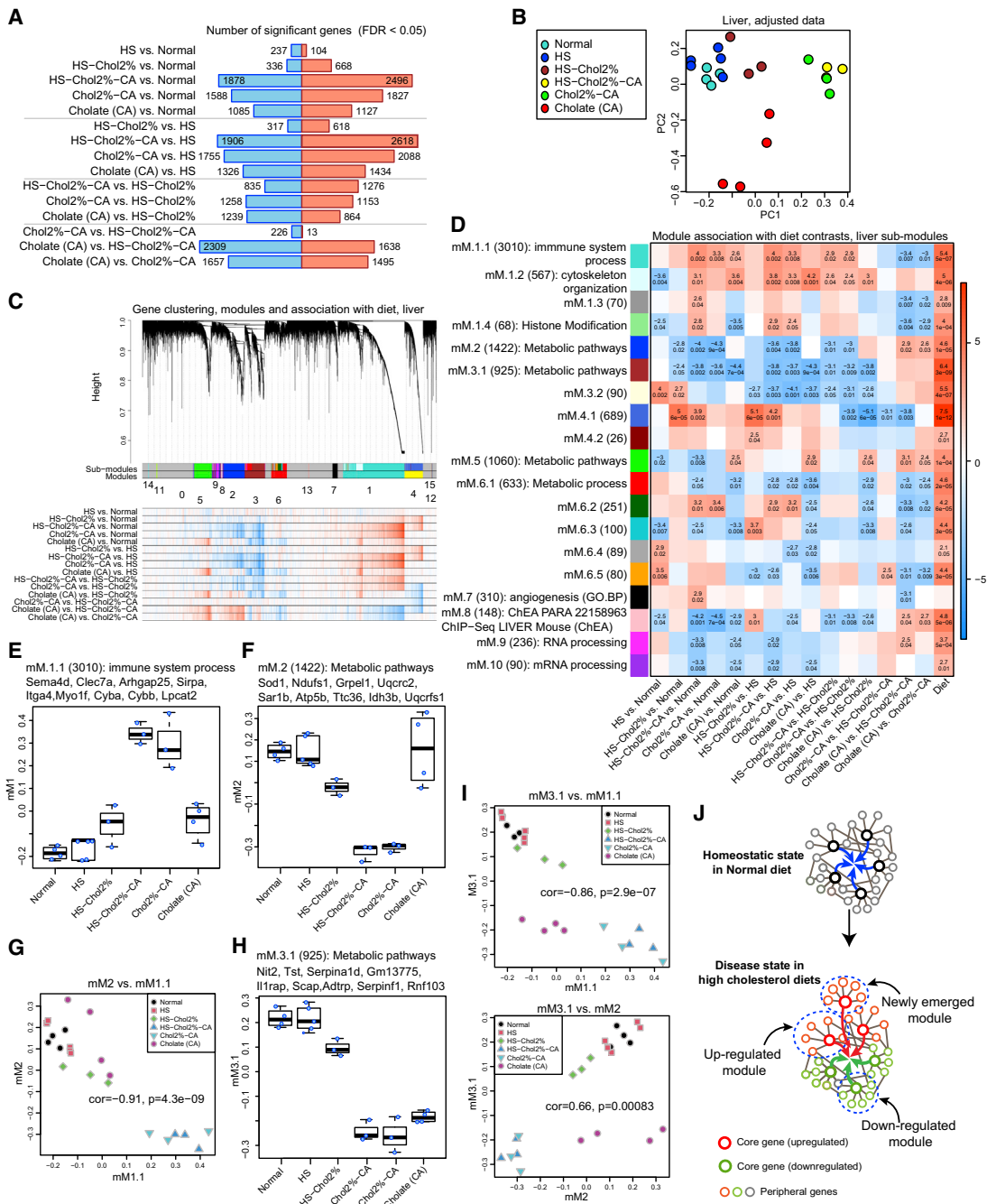


**Figure 2. Co-expression network analysis of mice liver and association of module eigengenes with diets**

(A) Numbers of significant (FDR < 0.05) differentially expressed genes for all 15 diet contrasts. Blue (red) represents down- or (up)regulated genes.

(B) Principal component (PC) plot showing the 2 leading PCs after outlier removal ( $n_{(\text{chol2\%\_ca})} = 1$ ) and adjustment for 1st surrogate variable (SV). Mice fed the HS\_Chol2%\_CA and Chol2%\_CA diets are closely clustered together. Each point represents one sample, color indicates diet.

(C) Gene clustering tree (dendrogram), module colors (main modules and submodules) and labels, and a heatmap of individual gene associations with diet contrasts. Numeric module labels are only shown for main modules. In the association heatmap, blue color indicates down- and red upregulation.

(D) Association of module eigengenes of selected submodules with diet contrasts and diet overall (last column). Each row corresponds to a module. Row labels indicate the numeric module label, module size, and top enrichment term (modules without enrichment labels are either not enriched significantly [Bonferroni-corrected  $p > 0.05$ ] or the module-gene set overlap represents less than 5% of the module genes). Color rectangles correspond to the module color in Figure 2C. Each column corresponds to either a diet contrast or overall diet as a factor. In the heatmap, numbers give the association significance Z statistic and the FDR estimate. For clarity, Z and FDR are only shown for those cells where FDR < 0.05. Color indicates strength and direction of the association Z.

(E and F) Expression of M1.1 and M2 across the 6 diets. Each box represents the interquartile range and the thick line in the box represents the median. Whiskers extend to the most extreme point that is no further than 1.5 times the interquartile range. Blue points show the actual expression values (one dot per sample); white

(legend continued on next page)

whose eigengene correlations were above 0.8, again approximating the WGCNA method.

We next evaluated the significance of overlaps of WGCNA modules with the 5 sets of test modules, with particular focus on modules mM1.1, mM2, mM3.1, and mM7 (angiogenesis). We find that each of the 4 modules overlaps strongly with one or a few modules in each of the additional networks (Figures S2A–S2E). The spectral clustering returned modules containing one that overlaps strongly with both M1.1 and M2 (which are anti-correlated in WGCNA) (Figure S2C). This is likely due to the fact that MODA networks are all unsigned and hence do not distinguish positive and negative correlations. Hence, we focused on the remaining 4 methods.

We calculated MEs of the additional modules and correlated them with eigengenes of WGCNA modules. We find that module pairs with strong overlaps have strong ( $\geq 0.96$ ) correlations. For each of the 4 WGCNA modules we next selected a corresponding module in each of the additional networks (Table S2).

The high ME correlations mean that testing of association with traits (diet contrasts) would lead to similar results. Finally, we also evaluated enrichment of the additional modules in the same reference gene sets that were used for enrichment analysis of the WGCNA modules. We find that enrichment p values of strongly overlapping modules are strongly correlated (Figures S3A–S3D). We thus conclude that the findings we obtained using WGCNA could be, to a large degree, recapitulated using other network analysis techniques. Having said that, none of the other network methods reproduces WGCNA results precisely. Among other reasons, this is because we used signed WGCNA in which negatively correlated genes are considered unconnected; all other methods in this comparison create unsigned networks in which the sign of the correlation is disregarded.

We next explored whether WGCNA co-expression modules are preserved between mice and human liver diseases. If true, this would suggest the existence of “core modules” across species.

#### WGCNA analysis of human fatty liver indicates the presence of similar co-expression modules with different behavior

Hepatic steatosis and steatohepatitis represent a spectrum of disease that is impacted by environmental and dietary queues (El-Agroudy et al., 2019). We investigated transcriptional changes in human fatty liver by performing WGCNA on human liver transcriptomic data of healthy, obese without MAFLD, MAFLD, and metabolic steatohepatitis (MeSH) patients (GEO dataset: GSE126848). Differential expression analysis demonstrated that MAFLD and metabolic steatohepatitis had a pro-

found impact on mRNA expression compared with healthy and obese, with 5,000 to 7,000 significant DE genes (Figure 3A). A far smaller number of about 200 genes were DE between obese and healthy (similar to that between normal chow and HS diets in mice), as well as between metabolic steatohepatitis and MAFLD. The dramatic effect of MAFLD and metabolic steatohepatitis is also observed in the PCA plot showing a relatively clean separation of samples by disease (MAFLD and metabolic steatohepatitis) (Figure 3B). DE Z statistics of the 4 contrasts with thousands of significant DE genes exhibited very high correlations indicating that the sets of DE genes are very similar. The correlation of DE Z statistics for obese versus healthy and metabolic steatohepatitis versus MAFLD was weaker (0.34) but still positive (Figure 3C).

WGCNA analysis of the human fatty liver data (Figure 3D) found two large branches and a handful of independent small branches (co-expression modules 5, 20, 11, 1, and 19). Although the large branches do exhibit some substructure (e.g., co-expression module 9 is relatively distinct), it is clear that most of the expression variation captured by WGCNA reflects differences between metabolic steatohepatitis and MAFLD on the one hand and healthy and obese on the other.

Of the 20 co-expression modules, 12 are associated with disease based on the overall F test  $FDR < 0.05$  (Figure 3E). Consistent with phenotypic data (Suppli et al., 2019), a module labeled human fatty liver module 11.1 (hfM11.1) was upregulated in metabolic steatohepatitis patients (Figure 3F), contains hub genes related to fibrosis (AEBP1, COL1A2, COL3A1, and LOXL4) and is enriched in extracellular matrix organization. Interestingly, two immune-related modules (hfM1 and hfM7.2) show opposite behavior. Modules hfM1 with hub genes such as CCR5, CD48, IL2RG, SLAM7, and SLAM8 was upregulated in metabolic steatohepatitis, while hfM7.2 with hub genes LAPTM5, ADA2, MARCH1, HCLS1, C3AR, WIPF1, PTAFR, and CD86 related to the innate immune response showed downregulation (Figure 3F). hfM1 was positively correlated with hfM11.1 related to fibrosis ( $cor = 0.62, p = 7.4e-07$ ); however, hfM7.2 was not ( $cor = -0.089, p = 0.53$ ) (Figure 3G).

It is known that chronic liver inflammation in metabolic steatohepatitis contributes to liver fibrosis. The high correlation between the upregulated immune module hfM1 and fibrosis (hfM11.1) suggests that hfM1 is related to inflammatory responses that drive fibrosis in metabolic steatohepatitis. In contrast, another module related to the immune response (hfM7.2) was downregulated. Interestingly, hfM7.2 demonstrated strong inverse correlation with upregulated hfM2 ( $cor = -0.81, p = 2.1e-13$ ), that is enriched in metabolic processes (Figures 3F and 3G); hfM1 was weakly correlated to hfM2 ( $cor = 0.28, p = 0.042$ ).

points duplicate the values beyond the range of the whiskers. For each plot, the title shows the enrichment label for the module (top enrichment terms) and the top hub genes (ordered by decreasing kME) in each module.

(G) Scatterplot of module eigengenes mM1.1 and M2.

(H) Expression of module eigengene mM3.1.

(I) Scatterplots of mM3.1 with mM1.1 and mM2.

(J) A network model of liver homeostatic perturbation in response to diets containing cholesterol and cholic acid. In this model, an altered homeostatic state is depicted as upregulation and downregulation of modules (e.g., immune response and metabolism, respectively). Each module consists of core genes and peripheral genes that either positively (red arrows) or negatively (green arrows) contribute to a phenotype.

(NC, normal chow,  $n_{(mice)} = 4$ ; HS, high sucrose,  $n_{(mice)} = 5$ ; HS\_Chol2%, high sucrose + high cholesterol (2%),  $n_{(mice)} = 3$ ; HS\_Chol2%\_CA, high sucrose + high cholesterol (2%) + cholic acid,  $n_{(mice)} = 3$ ; Chol2%\_CA, high cholesterol (2%) + cholic acid (CA),  $n_{(mice)} = 4$ , removed outlier = 1; CA: cholic acid,  $n_{(mice)} = 4$ )

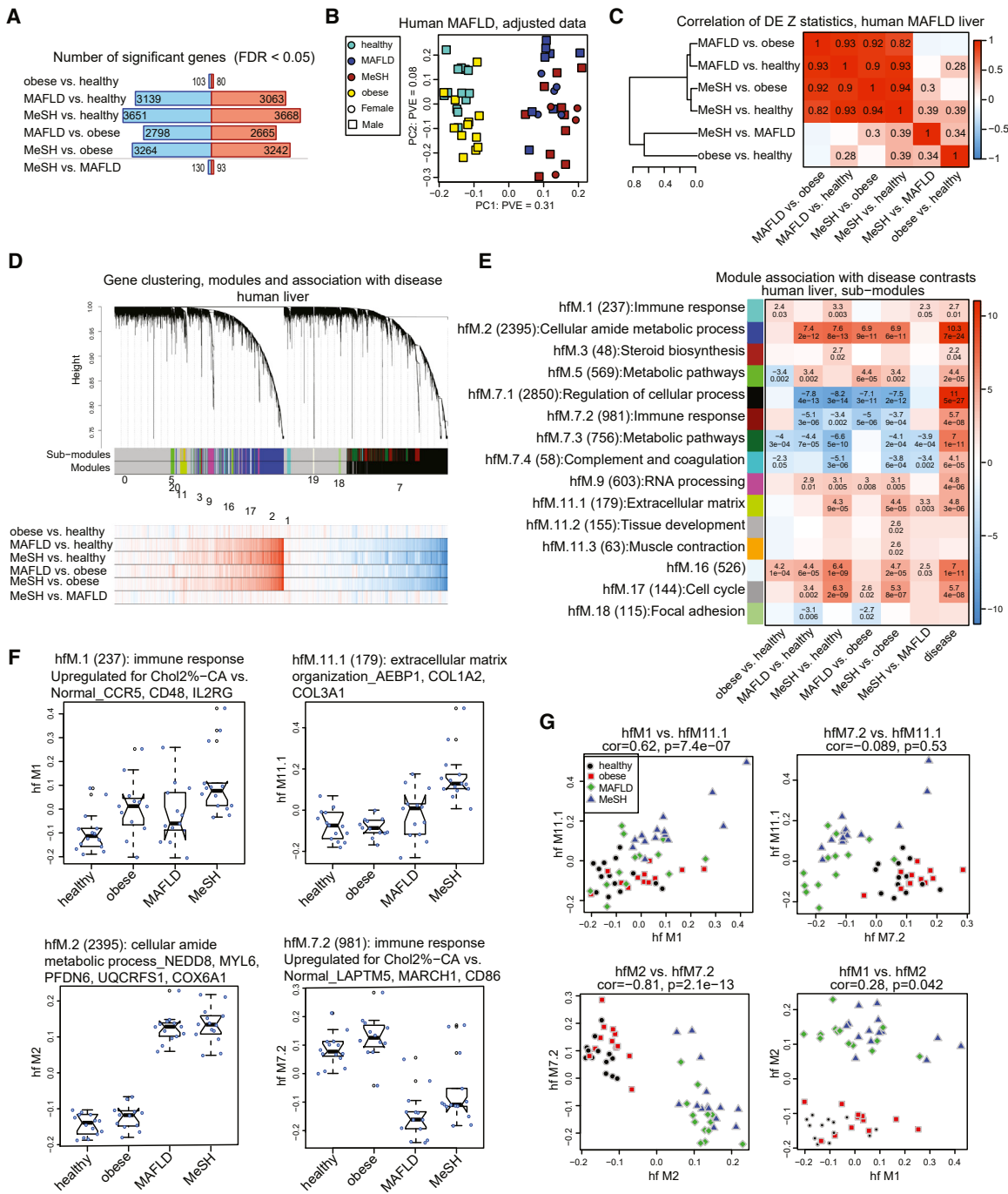


**Figure 3. Co-expression network analysis of human fatty liver and association of module eigengenes with disease (MAFLD/metabolic steatohepatitis)**

(A) Numbers of significant differentially expressed (FDR < 0.05) genes for all 6 disease contrasts. Blue (red) represents down- (up)regulated genes.

(B) PC plot showing the 2 leading PCs after outlier removal ( $n_{(\text{mafif})} = 2$ ;  $n_{(\text{mesh})} = 2$ ) and adjustment for leading 2 SVs. Each point represents one sample.

(C) Correlations of individual gene differentially expressed Z statistics for the 6 contrasts tested in the human liver data. Only correlations with absolute value > 0.2 are shown explicitly.

(D) Gene clustering tree (dendrogram), module colors and labels, and a heatmap of individual genes association with disease contrasts. Numeric module labels are only shown for main modules. In the association heatmap, blue color indicates downregulation and red upregulation.

(E) Association of module eigengenes of selected submodules with disease contrasts and disease overall (last column). Each row corresponds to a module. Row labels indicate the numeric module label, module size, and top enrichment term (hM16 is enriched for unfolded protein response but the module-gene set overlap represents less than 5% of the module genes). Color rectangles correspond to the module color in Figure 3D. Each column corresponds to either a disease

(legend continued on next page)  
Cell Systems 12, 432–445, May 19, 2021 437

In sum, human fatty liver module 1 (immune response) shows similar behavior to mouse module 1 related to the immune response in mice, and both are upregulated. In contrast, human module 7.2 (immune response) was downregulated and module 2 (metabolic processes) was upregulated. These 2 human co-expression modules demonstrate opposite behavior to mouse M1 (immune response) and mouse M2 (metabolism), respectively.

### Concordance of DE genes and module preservation points to existence of core modules between species

We envisaged that core homeostatic processes should be similar between species and might help in understanding homeostatic perturbations in humans. We therefore evaluated concordance of DE genes in human fatty liver disease with DE for various diet contrasts in mice. We first calculated genome-wide correlations of DE Z statistics of mapped genes (Figure 4A) and observed several correlations with absolute values between 0.2 and 0.3. We calculated enrichment of DE genes in human data for DE genes in the mouse data. The overlap counts and enrichment p values are shown in Figure 4B. We found statistically significant overlaps of several DE sets. The highest number of overlapped genes was detected between DE sets that were downregulated in human MAFLD and metabolic steatohepatitis (versus normal or obese) and upregulated in HS\_Chol2%\_CA and Chol2%\_CA diets (versus NC or HS diet) (Figure 4B).

Next, we calculated preservation statistics (Langfelder et al., 2011) of human and mouse co-expression modules in the respective complementary dataset with the corresponding modules as test modules. Module preservation calculations result in multiple observed and permutation-based significance statistics. It is often convenient to summarize these into a single (or just a few) summary measures. One useful summary measure is Zsummary, a summary of permutation-based preservation Z statistics. Mouse module mM7 (angiogenesis) has the highest Zsummary preservation statistic ( $Z = 18.6$ ), followed by mM1.1 (immune response,  $Z = 12.3$ ), mM2 (metabolic pathways,  $Z = 9.92$ ), and mM9 (RNA processing,  $Z = 8.42$ ) (Figure 4C). These four modules can be viewed as showing strong evidence of module preservation between species ( $Z \geq 8$ ). Module mM6.3 shows moderate evidence of preservation ( $8 \geq Z \geq 4$ ) while the remaining modules show either weak ( $Z = 3.5$  for mM6.2) or no evidence of preservation (e.g.,  $Z = -0.4$  for mM5).

Results of the converse module preservation study are shown in Figure 4D. We find that immune-response-related modules hfM7.2 ( $Z = 39.6$ ) and hfM1 ( $Z = 26.3$ ) and a module related to steroid biosynthesis (hfM3,  $Z = 14.1$ ) show the strongest evidence of preservation, while modules hfM18 (focal adhesion,  $Z = 10.9$ ), hfM17 (cell cycle,  $Z = 11$ ), hfM11.1 (extracellular matrix organization,  $Z = 8.98$ ), and hfM5 (metabolic pathways,  $Z = 8.44$ ) show

borderline strong evidence of preservation. Modules hfM2 (cellular amide metabolic processes,  $Z = 6.84$ ) and hfM7.1 (regulation of cellular processes,  $Z = 4.97$ ) show moderate evidence of preservation, and the rest either weak or no evidence of preservation.

To provide a more intuitive picture of module preservation, we calculated module overlaps of mouse and human submodules (Figure 4E); we found that the module related to immune response in mouse (mM1.1) overlaps significantly with human hfM1, hfM7.2, hfM11.1, hfM17, and hfM18. Interestingly, human hfM2, hfM3, and hfM5 linked to metabolic pathways highly overlap with mouse modules related to metabolic pathways (mM2 and mM3.1) (Figure 4E).

Thus, similar to the mouse homeostatic perturbation model (Figure 2J), human modules that overlap with mouse immune response (mM1.1) and metabolism (mouse mM2, mM3.1) could act as core modules representing homeostasis perturbation in human fatty liver (Figure 4E). Hence, we defined human hfM1, hfM7.2, hfM11.1, hfM17, and hfM18 (linked to mouse immune module 1.1) and metabolic-related hfM2, hfM3, and hfM5 as core modules that are perturbed in human fatty liver disease. In addition, mouse mM7 (small module with a high preservation score) that overlaps with human hfM7.1 (large module with moderate preservation) can be added to the core system in mice and humans, respectively (Figures 4C–4E). It is noteworthy that the direction of changes of some of these co-expression modules are different between mice (especially in high cholesterol and CA-fed groups) and humans and the phenotypic outcome in mice might thus be divergent from human fatty liver disease (Figures 2D, 3E, and 4F).

### WGCNA analysis of TCGA liver cancer data confirms preservation of core modules between mice, human fatty liver, and human liver cancer

We surmised that if the core modules are essential for homeostasis, then their deregulation should be a feature of other liver-related disorders. To explore this concept, we used liver cancer as it should have divergent transcriptomic signatures from mice dietary models and human fatty liver. We performed WGCNA on 3 independent human liver cancer datasets: The cancer genome atlas (TCGA) dataset (LIHC-US, 345 cases), and 2 International Cancer Genome Consortium (ICGC) datasets from France (LICA-FR, 160 cases) and Japan (LIRI-JP, 445 cases). Subsequently, we performed preservation analysis and explored human liver cancer (hc) co-expression modules that have overlap with mice and human MAFLD core modules.

We calculated preservation statistics of mouse modules in the respective TCGA and ICGC data and vice versa (Figures 5A and S4, see also supplemental data on Mendeley: <https://doi.org/10.17632/sfng2h249n.1>). Based on the Zsummary statistic, the

contrast or overall disease as a factor. In the heatmap, numbers give the association significance Z statistic and the FDR estimate. For clarity, Z and FDR are only shown for those cells where FDR < 0.05. Color indicates strength and direction of the association Z statistic.

(F) Expression of module eigengenes hfM1, hfM2, hfM7.2, and hfM11.1 across the 4 sample groups. Each box represents the interquartile range and the thick line in the box represents the median. Whiskers extend to the most extreme point that is no further than 1.5 times the interquartile range. Blue points are the actual expression values (one dot per sample); white points duplicate the values beyond the range of the whiskers. For each plot, the title shows the enrichment label for the module (top enrichment terms) and the top hub genes (ordered by decreasing kME) in each module.

(G) Scatterplots of module eigengenes show positive correlation between hfM11.1 and hfM1 and negative correlation between hfM7.2 and hfM2. Number of samples after outlier removal = 53 ( $n_{(\text{healthy})} = 14$ ;  $n_{(\text{obese})} = 12$ ;  $n_{(\text{mafld})} = 13$ ;  $n_{(\text{mesh})} = 14$ ). See also supplemental information.

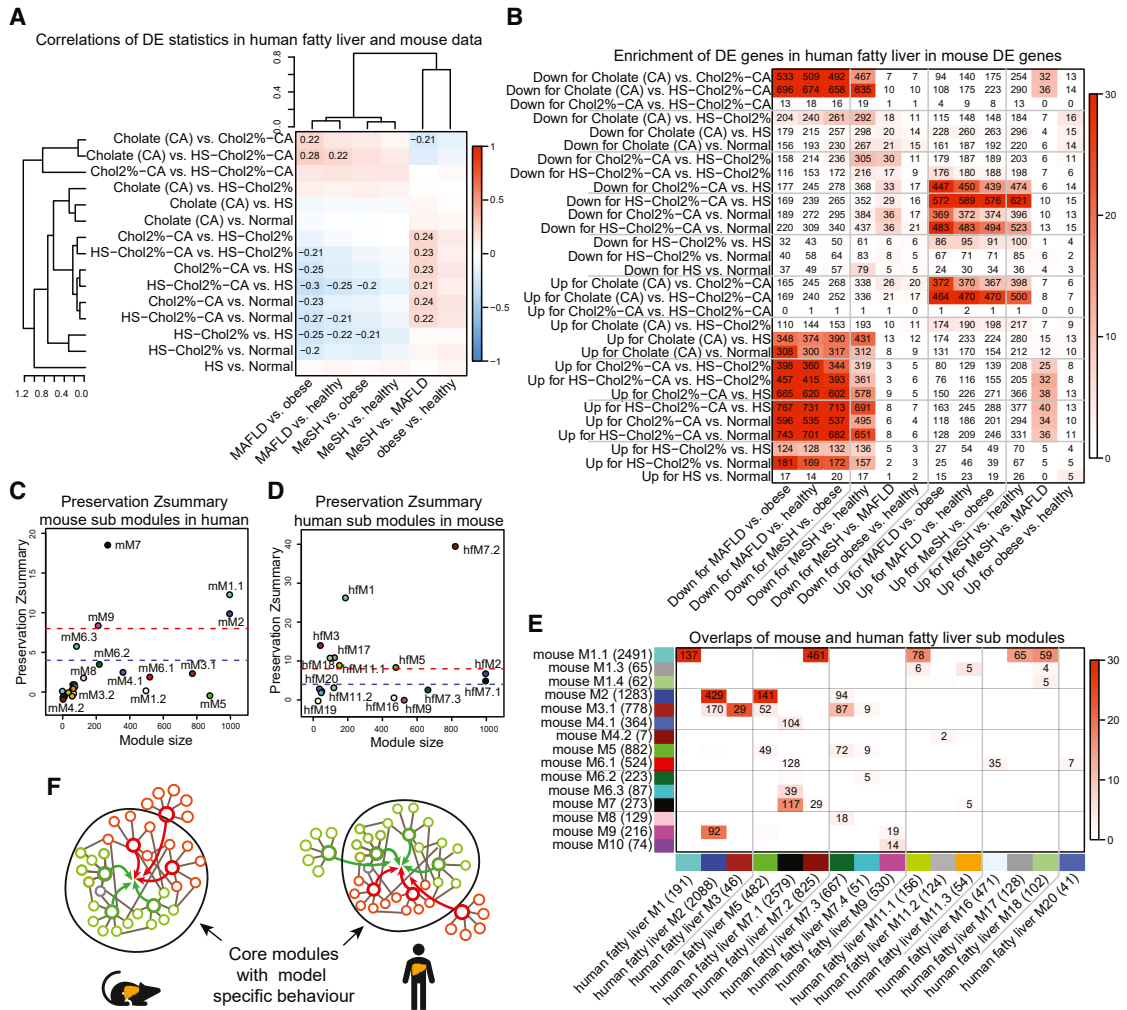


**Figure 4. Module preservation between mice and human fatty liver disease**

(A) Correlations of DE Z statistics for disease/condition contrasts in human data (columns) with Z statistics for diet contrasts in mouse data. Clustering trees of both sets of statistics are based on correlations of Z statistics within each set.

(B) Overlaps of significantly (FDR < 0.05) DE genes in condition contrasts in human liver data (columns) in DE genes for diet contrasts in mouse liver data (rows). Numbers indicate the numbers of overlapping genes; color represents negative  $\log_{10}$  of the hypergeometric enrichment p value. For clarity, the color scale is truncated at 30.

(C and D) Preservation Zsummary statistics of mouse submodules in human data and human submodules in mouse data. Each point represents a module. Point color reflects the module color as used in Figures 3D and 3E of human; Figures 2C and 2D of mouse data; where possible, points are also labeled by the numeric label of the module. Blue and red lines depict the rough thresholds for moderate ( $Z = 4$ ) and strong ( $Z = 8$ ) evidence of module preservation.

(E) Overlaps of mouse and human modules. Each module is labeled by organism, module label, color and number of genes (after mapping mouse Entrez IDs to human and restricting both data sets to common Entrez IDs). Numbers in the table give the overlap size (number of common genes) while color represents  $-\log_{10}$  of the hypergeometric enrichment p value.

(F) Schematic depicts that in mice challenged with diets containing cholesterol and cholic acid, the behavior of the core system differs (diverges) from human MAFLD/metabolic steatohepatitis.

core modules, namely mouse modules mM1.1 (immune response), mM2 and mM3.1 (metabolic pathways), and mM7 (angiogenesis) are strongly preserved ( $Z \geq 8$ ) in human liver cancer (Figure 5A). Results of the converse module preservation study indicates that each of the liver cancer datasets contains a single extremely highly preserved co-expression module related to immune responses (hcM1 in LICA-FR and LIHC-US, and hcM7 in LIRI-JP) and several other modules whose preservation is strong but not as high (Figure S4). The heatmap representation of module overlap of mouse submodules in LIHC-US

and converse module preservation are demonstrated in Figures 5B and S4A. It shows that mouse immune response (mM1) has overlap with: tumor immune response (hcM1 in LIHC-US), extracellular matrix organization (hcM11 in LIHC-US), cell cycle (hcM17 in LIHC-US), focal adhesion (hcM18 in LIHC-US), and cell development (hcM38 in LIHC-US). In addition, mouse mM2 (metabolic pathways) highly overlapped with hcM2 (RNA binding), and metabolic pathways (hcM5.1, and hcM5.3) in the LIHC-US human tumor dataset. Likewise, mouse mM3 (metabolic pathways) overlapped with hcM5.1 and hcM5.3 in the

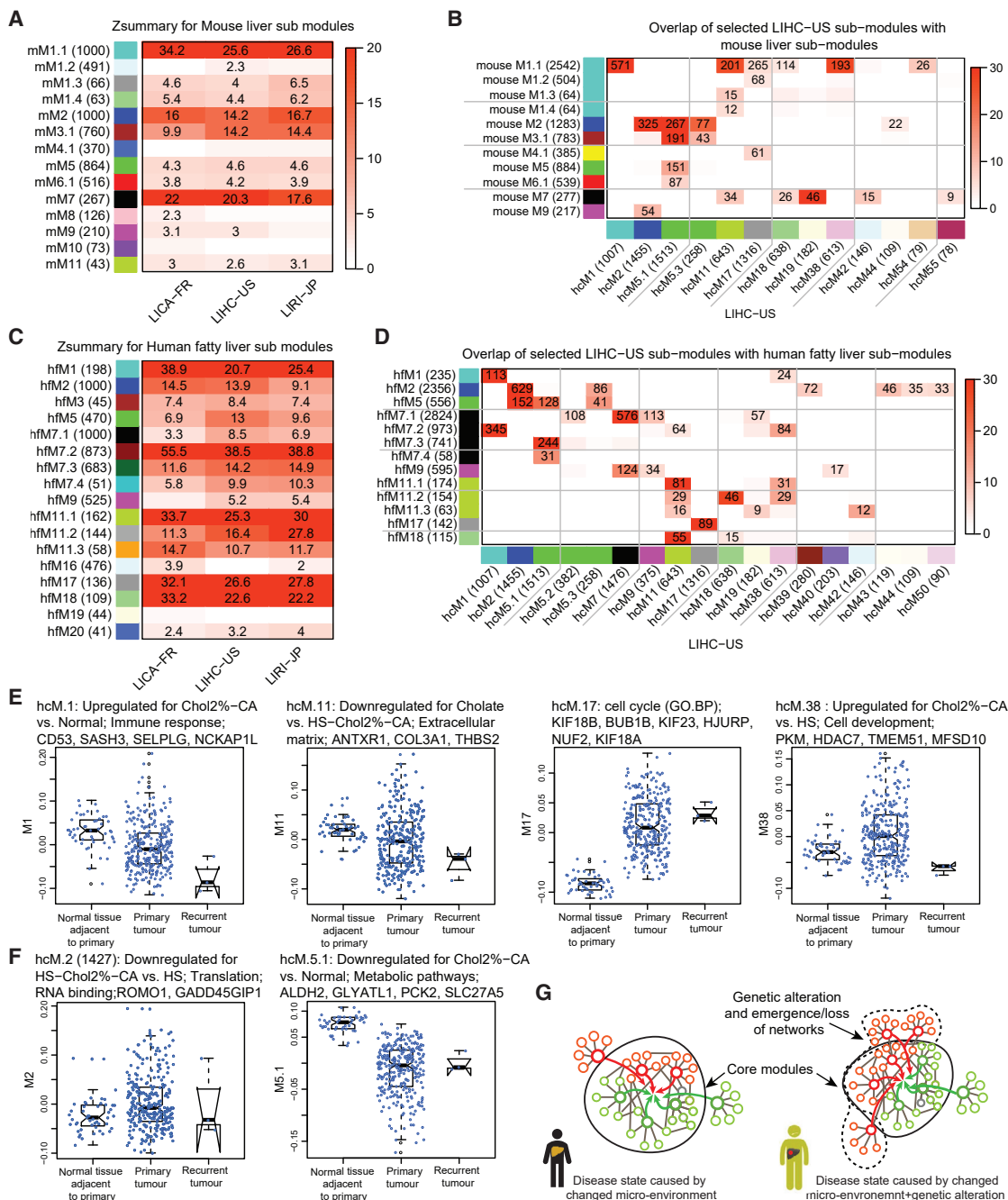


**Figure 5. Module preservation analysis between mice, human fatty liver, and human liver cancer datasets and preserved module behavior in LIHC-US dataset**

- (A) Heatmap representation of module preservation Zsummary statistics of selected mouse submodules in the liver cancer data.
- (B) Overlaps of mouse modules with LIHC-US liver cancer modules. Each module is labeled by module label, color, and number of genes (after mapping mouse Entrez IDs to human and restricting both datasets to common Entrez IDs). Numbers in the table give the overlap size (number of common genes) while color represents  $-\log_{10}$  of the hypergeometric enrichment p value.
- (C) Heatmap representation of module preservation Zsummary statistics of selected human fatty liver submodules in liver cancer data.
- (D) Overlaps of human fatty liver modules with LIHC-US dataset.
- (E) Expression of module eigengenes of TCGA LIHC-US modules (hcM1, hcM11, hcM17, and hcM38) that overlap with mouse mM1.1 (immune response).
- (F) Expression of module eigengenes of TCGA LIHC-US modules (hcM2 and hcM5.1) that overlap with mouse mM2 and mM3.1 (metabolic pathways). Each point represents a sample,  $n = 344$  ( $n_{\text{Normal tissue adjacent to primary}} = 48$ ;  $n_{\text{Primary tumour}} = 293$ ;  $n_{\text{Recurrent tumour}} = 3$ ); we excluded 1 sample (outlier) in LIHS\_US dataset.
- (G) A network model of liver homeostatic perturbation in human MAFLD and liver cancer. Here, core homeostatic perturbation is depicted as down- or upregulation of core modules (e.g., immune response and metabolism). Incorporating non-core modules can provide a better picture of diseases. E.g., in cancer, adding modules secondary to genetic alterations might explain some of the effects on gene regulatory networks (GRNs) and homeostatic state of tumor. See also Figures S4 and S5.

LIHC-US human tumor dataset. Finally, mouse mM7 (angiogenesis) is represented in hcM19 (vascular development) in the LIHC-US human tumor dataset. In sum, we could demonstrate preserved modules in liver cancer that overlap with mice core modules (immune response, metabolic pathways, and angiogenesis).

To validate the components of these core systems, we examined whether similar modules are preserved between human fatty liver and liver cancer. Indeed, human fatty liver module 7.2 (hfM7.2) related to the immune response showed the highest preservation score with 3 independent liver cancer datasets followed by hfM1 (immune response), hfM11 (extracellular matrix organization), hfM17 (cell cycle), and hfM18 (Focal adhesion). In addition, human fatty liver modules hfM2, hfM3, and hfM5 (metabolism) are preserved in all liver datasets (Figures 5C and 5D). Overall, these observations indicate that similar to mice homeostasis perturbation in high cholesterol and CA diets, the core homeostatic disturbance in human HCC and human fatty liver can be depicted by preserved modules. We termed these modules as “core modules.”

Considering that the direction and behavior of modules could have implications for disease outcomes, we examined the direction of these modules in LIHC-US tumors compared with adjacent normal tissue (Figures 5E and 5F). Interestingly, downregulation of hcM1 (immune response), hcM5.1 (metabolic pathways), and hcM11 (extracellular matrix organization), and upregulation of hcM2 (translation and RNA binding), hcM17 (cell cycle), and hcM38 (cell development) was observed in tumors compared with adjacent normal tissue. Thus, these core modules and the direction of their response can provide a picture of the core homeostatic state of tumors.

Of interest in the LIHC\_US dataset, about 12,000 genes were DE between tumor and non-tumor liver, a much larger number than the DE genes in mice and human fatty liver datasets (Figures 2A, 3A, and S5A). As might be expected, WGCNA in liver cancer identified a higher number of modules than in mice diets or human fatty liver datasets, including modules that were enriched for genomic positions (Figures S5B and S5C). This could be indicative of genomic alterations such as copy-number variations (CNVs) or alterations in regulatory mechanisms that lead to emergence of new co-expression modules in cancer. Of note, non-core module hcM43 (enriched in genes near 152.5 Mb on Chr1, cor = 0.43, p = 3e-14) and core module hcM17 (cell cycle, cor = 0.41, p = 3e-13) are the two modules with the strongest association with the fraction of the genome altered (Figure S6). We surmise that alterations in core modules can provide a picture of core homeostatic perturbation mechanisms; however, adding “non-core modules” such as emerged co-expression modules specific to cancer (non-preserved modules) could provide a more nuanced picture of the homeostatic perturbations (Figure 5G).

### Can the behavior of modules predict cancer outcomes?

Besides the presence of disease-related modules (core and non-core), we hypothesized that the response of modules could play a role in patient outcomes. We therefore looked for co-expression modules that were predictive of survival in the LIHC-US dataset. Subsequently, we undertook further analysis to find genes that could regulate the behavior of these

modules related to survival to provide mechanistic insights (Figure 6A).

To examine which modules are predictive of patient survival, we proceeded with the analysis in two phases, unstratified and stratified. In the unstratified phase, survival data were regressed against ME values using a Cox proportional hazard model (Therneau and Grambsch, 2000). Modules for which the model had  $p \leq 0.05$  were passed to the stratified phase. A log-rank p value for survival differences between the strata was calculated for each module subject to stratified analysis. The details can be found in methods and Figure S7A. Co-expression modules 38 and 17 had the strongest survival differences by a variety of methods. Kaplan-Meier (KM) plots for stratified submodules hcM5.1, hcM17, and hcM38 based on the Z score values are shown in Figure 6B.

Next, we explored the possibility of finding a module eigen-gene quantitative trait loci (module-eQTL) that could regulate the behavior of modules predictive of survival (hcM5.1, hcM17, and hcM38). Since hcM17 and hcM38 overlap with the immune module (mM1.1) in the mice dataset, we restricted analysis to germline variants. It is known that immunity-related genes are under strong germline genetic control (Lim et al., 2018; Quach et al., 2016). We therefore used germline variants that were *cis* eQTLs for genes in TCGA liver cancer (LIHC\_eQTL) dataset (Lim et al., 2018). We also investigated whether eQTLs that regulate immune-related modules regulate the preserved correlated metabolic module hcM5.1 (covariance in gene regulation). We classified sample genotypes as the reference allele homozygous, alternate/reference allele heterozygous, or alternate allele homozygous. We applied two methods: (1) a three-way ANOVA and (2) a linear model. Single-nucleotide polymorphisms (SNPs) that were significant at an FDR of 5% in both analyses were considered module-eQTLs (Figures S7B–S7D).

As expected, we found module-eQTLs that coordinately regulate hcM17 and hcM5.1 modules such as rs2298167, which is *cis* eQTL for CGN (effect size  $[\beta] = -0.74$ ,  $p = 9.16e-06$ ), and rs758097 that is *cis* eQTL for ZNF419 (effect size  $[\beta] = -0.71$ ,  $p = 1.72e-07$ ) and ZNF551 (effect size  $[\beta] = -0.52$ ,  $p = 2.64e-06$ ) (Figures 6C and S7D). Both rs2298167-G allele and rs758097-A allele are associated with higher expression of CGN and ZNF419, downregulation of hcM17, and upregulation of hcM5.1 (Figures 6C, 6D, S7E, and S7F). We did not find a module-eQTL for hcM38.

In addition, we discovered rs8076470, which is *cis* eQTL for SPATA20 (effect size  $[\beta] = -0.63$ ,  $p = 9.16e-06$ ) as a module-eQTL for hcM17 and for hcM5.1 at  $q < 0.2$  (Figures 6C and S7B). Of interest, higher bile levels of SPATA20 have been proposed as a biomarker for cholangiocarcinoma (Shen et al., 2012). The rs8076470-T allele is associated with lower expression of SPATA20, downregulation of hcM17 (negative coefficient of -0.016), and (probably, though less definitive), upregulation of hcM5.1 (positive coefficient of 0.013) (Figures 6C–6E, S7B, and S7C). There was hardly any influence of ancestry, age, or sex to explain the variance in SPATA20 expression (Figure S7G) [https://albertlab.shinyapps.io/tcga\\_eqtl/](https://albertlab.shinyapps.io/tcga_eqtl/). However, a big impact of the top eQTL (rs8076470) and hidden factors measured by probabilistic estimation of expression residuals (PEER) (Stegle et al., 2012) is noticeable (Figure S7G). Interestingly, the

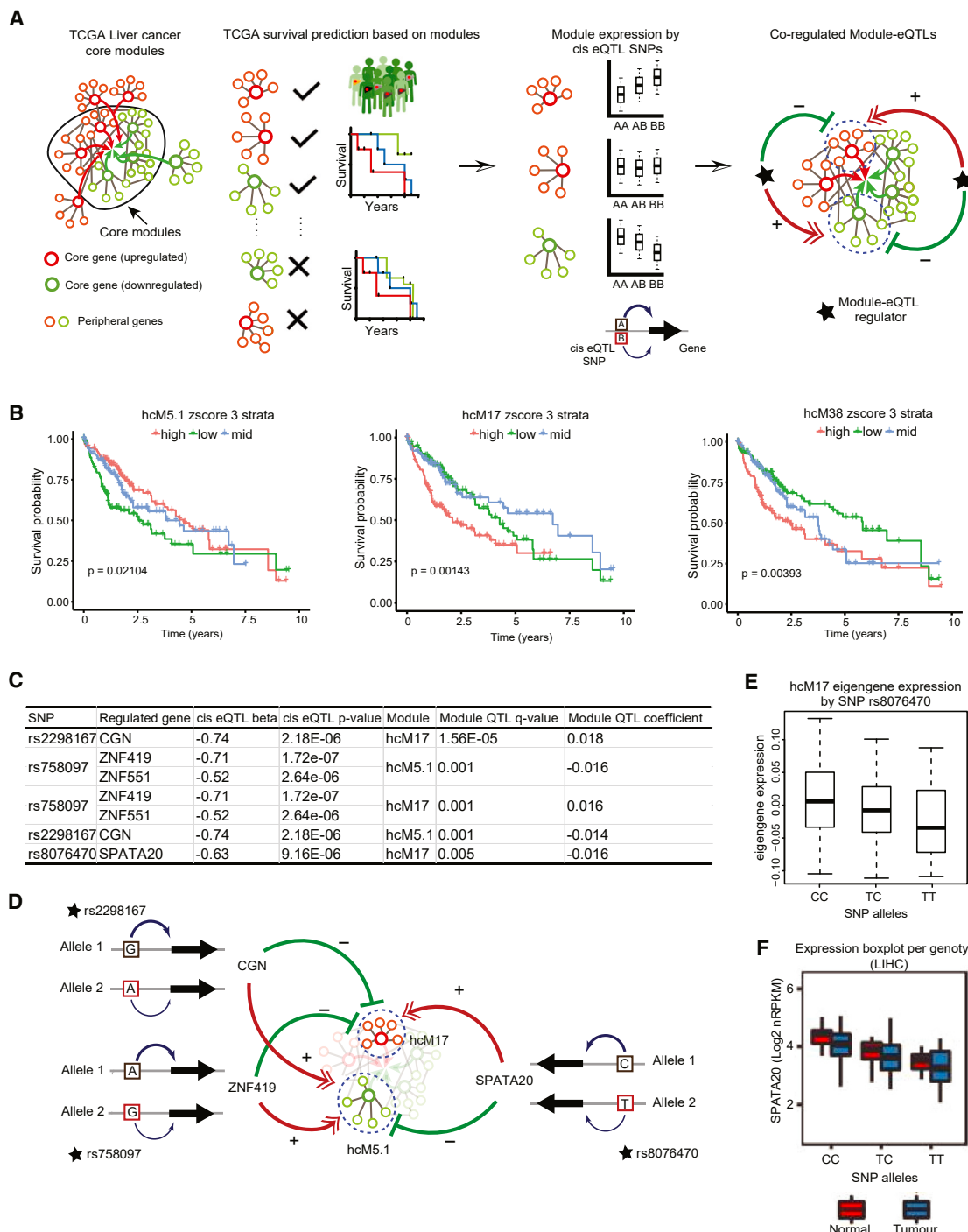


**Figure 6. Module-eQTLs explain the genetic covariance between negatively co-regulated modules predictive of patient survival**

(A) A framework workflow to investigate the effect of genetic variations on behavior of modules and the impact on patient survival in liver cancer.

(B) Lower expression of hcM5.1 and higher levels of hcM17 and hcM38 were negatively correlated with survival.

(C and D) Summary of SNPs in *cis* eQTL to genes that are associated with expression levels of hcM5.1 and hcM17. No module-eQTLs were found for hcM38. The variant associated with lower expression of CGN (effect size  $\beta$  of the association  $-0.74$ ), is associated with higher expression of module 17 (positive coefficient of  $0.018$ ), and lower expression of module 5.1 (negative coefficient of  $-0.014$ ). The variant associated with lower expression of ZNF419 and ZNF551 (effect size  $\beta$  of the association  $-0.71$  and  $-0.52$ , respectively) is associated with higher expression of hcM17 (positive coefficient of  $0.016$ ) and lower expression of hcM5.1 (negative coefficient of  $-0.016$ ).

(D and E) rs8076470 variant associated with lower expression of SPATA20 is associated with lower expression of hcM17. ( $n_{\text{subjects with available survival and genotype data}} = 291$ )

(F) Both normal liver and tumors show the effect of rs8076470 on SPATA20 expression. See also Figure S7.

rs8076470 *cis* eQTL effect is true in normal tissue and not just in tumors (Figure 6E).

Overall, besides environmental effects, our module-eQTLs analysis indicates that genetic variations can impact the behavior of modules and hence influence homeostasis. We also demonstrated a covariance in regulatory mechanisms that could be exploited to simultaneously target two dysregulated modules to improve patient outcomes in cancer or fatty liver disease. The new candidate therapeutic options merits further analysis and functional studies.

## DISCUSSION

We applied systems biology and network analysis methods on genome-wide liver transcriptome data to model perturbations of the homeostatic state in mouse liver resulting from variations in dietary composition. The data were then compared with human fatty liver and liver cancer. We demonstrated high preservation of co-expression modules of genes related to the immune response and metabolism between mice, humans with fatty liver and patients with liver cancer. We defined the modules of genes that are preserved in all three datasets as “core modules.” Interestingly, besides the appearance of core modules, the response (direction of changes) of modules varied between mice and humans with fatty liver disease with downregulation of metabolic pathways (mM2) in mice and upregulation of mM2 and mM5 in human fatty liver. Conversely, the immune response in mice was upregulated; however, in human fatty liver, two immune modules mM1 and mM7.2 emerged that showed a divergent response (up- and downregulation, respectively). Together, this suggests that the consequences of insults/stress to organs such as the liver (for example, through diet or the development of obesity and insulin resistance) can be contemplated as alterations in core modules that also have disease/model specific responses (up- or downregulation).

In addition to core modules, non-core modules (enriched but not preserved) provide a more comprehensive, disease-specific detail of altered homeostasis. For example, upregulation of the unfolded protein response (enriched in mM16 but with a small overlap of less than 5% of the module genes) in human fatty liver has been linked to liver steatosis (Friedman et al., 2018; Kim et al., 2018). However, this module is not preserved in our mice and liver cancer datasets. Interestingly, the diversity of co-expression modules increases in liver cancer with emergence of new co-expression modules (non-core modules) such as modules enriched in genomic positions (hcM43-50). This could be related to alterations in gene regulatory networks, CNV, or transcription factor binding in cancer (Lee and Young, 2013). Emergence of these non-core modules especially in cancer represent a further deviation from the homeostatic state that could have pushed the system from non-tumor disease toward a tumor state.

Apart from the components of core and non-core modules, the response of modules is important in determining outcomes. For example, upregulation of some core modules such as cell cycle (hcM17), cell development (hcM38), and downregulation of metabolic pathways (hcM5.1) was predictive of poor survival in the LIHC-US dataset. Indeed, we found multiple module-eQTLs that coordinately regulate cell cycle (hcM17) and metabolic path-

ways (hcM5.1). Further, genetic variation with lower expression of CGN, ZNF419, and ZNF551 was associated with upregulation of cell cycle (hcM17) and downregulation of metabolic pathways (hcM5.1). On the other hand, a genetic variant that led to higher expression of SPATA20 positively regulated expression of cell cycle (hcM17) and negatively metabolic pathways (hcM5.1). This suggests that increasing the expression of CGN, ZNF419, and ZNF551 or reducing that of SPATA20 might favorably alter the behavior of core modules and improve outcomes in liver cancer and should be investigated in experimental systems.

It is accepted that combinatorial therapy is necessary for treatment of most diseases (Sun et al., 2013). Conceivably, in a specific disease (e.g., MAFLD), identifying and validating core genes and module-eQTLs for all disease modules can add to the therapeutic arsenal. A coordinated targeting of core genes might thus have global effects on networks of gene expression and work toward restoring homeostasis/improve outcomes. Considering that the majority of disease modules in fatty liver overlap with cancer modules and the availability of multi-omics cancer datasets, we propose that our framework can find new therapeutic targets for fatty liver disease.

In conclusion, pre-clinical models do not always resemble the spectrum of human disease. These inter-species differences (i.e., between mice and humans) have led to efforts to develop more relevant pre-clinical models (Febbraio et al., 2019). In this work, despite these dissimilarities, we highlight a framework for using pre-clinical models to understand fatty liver and liver cancer pathogenesis. In addition, we provided a network concept for understanding homeostatic perturbations and a strategy to modulate core network modules to improve patient outcomes.

## STAR★METHODS

Detailed methods are provided in the online version of this paper and include the following:

- [KEY RESOURCES TABLE](#)
- [RESOURCE AVAILABILITY](#)
  - Lead contact
  - Materials availability
  - Data and code availability
- [EXPERIMENTAL MODEL AND SUBJECT DETAILS](#)
  - Mice
- [METHOD DETAILS](#)
  - Histology
  - Hepatic non-parenchymal cell isolation and flow cytometry
  - RNA\_Seq
- [QUANTIFICATION AND STATISTICAL ANALYSIS](#)
  - Statistical analysis of phenotypic data
  - Flow cytometry analysis
  - WGCNA, enrichment, and preservation analysis
  - Transformation of data for WGCNA
  - Differential expression analysis
  - Concordance of DE between mice and human fatty liver
  - Enrichment of sets of DE genes
  - Weighted gene co-expression network analysis

- Association of modules with diet, fatty liver, or traits
- Module preservation between human and mouse data
- Enrichment calculations in PPI pairs from BioGRID and STRING databases
- Network construction using MODA, ARACNE and MRNET
- Module survival stratification
- Module eigengene quantitative trait loci (Module-eQTL)

#### SUPPLEMENTAL INFORMATION

Supplemental information can be found online at <https://doi.org/10.1016/j.cels.2021.04.004>.

#### ACKNOWLEDGMENTS

The results published here are in part based upon data generated by The Cancer Genome Atlas managed by the NCI and NHGRI. Information about TCGA can be found at <http://cancergenome.nih.gov>. We would also like to acknowledge the clinical contributors and the data producers from the ICGC who have generated the liver cancer datasets and made them available for public analysis. This work was supported by a National Health and Medical Research Council of Australia (NHMRC) grant APP1108422. J.G. and S.E. are supported by the Robert W. Storr Bequest to the Sydney Medical Foundation, University of Sydney; and NHMRC program grants (APP1053206 and APP1196492). Flow cytometry and histology were performed at the Westmead Scientific Platforms, which are supported by the Westmead Research Hub, the Westmead Institute for Medical Research, the Cancer Institute New South Wales, the National Health and Medical Research Council and the Ian Potter Foundation. We acknowledge Dr. Ross Matthews and Westmead Research holding and Virginia James in the Department of Histology for their contributions to this work.

#### AUTHOR CONTRIBUTIONS

Conceptualization, S.E.; methodology, S.E., T.G.B., and P.L.; project administration, S.E. and T.G.B.; resources: S.E., T.G.B., and V.H.; investigation, S.E., M.K.A., M.R.-M., V.H., G.A.T., S.D., and H.G.; formal analysis, P.L., T.G.B., D.D., D.V., and C.L.; visualization, P.L., S.E., D.V., and B.S.G.; data curation, S.E., T.G.B., and P.L.; writing – original draft, S.E.; writing – review & editing, J.G., P.L., T.G.B., and S.E.; funding acquisition; S.E., C.L., and J.G.; supervision, J.G.

#### DECLARATION OF INTERESTS

The authors declare no competing interests.

Received: May 4, 2020

Revised: November 16, 2020

Accepted: April 9, 2021

Published: May 5, 2021

#### REFERENCES

- Alexander, M., Loomis, A.K., van der Lei, J., Duarte-Salles, T., Prieto-Alhambra, D., Ansell, D., Pasqua, A., Lapi, F., Rijnbeek, P., Mosseveld, M., et al. (2019). Risks and clinical predictors of cirrhosis and hepatocellular carcinoma diagnoses in adults with diagnosed NAFLD: real-world study of 18 million patients in four European cohorts. *BMC Med* 17, 95. <https://doi.org/10.1186/s12916-019-1321-x>.
- Chen, E.Y., Tan, C.M., Kou, Y., Duan, Q., Wang, Z., Meirelles, G.V., Clark, N.R., and Ma'ayan, A. (2013). Enrichr: interactive and collaborative HTML5 gene list enrichment analysis tool. *BMC Bioinformatics* 14, 128. <https://doi.org/10.1186/1471-2105-14-128>.
- Chou, C.H., Shrestha, S., Yang, C.D., Chang, N.W., Lin, Y.L., Liao, K.W., Huang, W.C., Sun, T.H., Tu, S.J., Lee, W.H., et al. (2018). miRTarBase update 2018: a resource for experimentally validated microRNA-target interactions. *Nucleic Acids Res* 46, D296–D302. <https://doi.org/10.1093/nar/gkx1067>.
- DeGregori, J. (2017). Connecting cancer to its causes requires incorporation of effects on tissue microenvironments. *Cancer Res* 77, 6065–6068. <https://doi.org/10.1158/0008-5472.CAN-17-1207>.
- Dobin, A., Davis, C.A., Schlesinger, F., Drenkow, J., Zaleski, C., Jha, S., Batut, P., Chaisson, M., and Gingeras, T.R. (2013). STAR: ultrafast universal RNA-seq aligner. *Bioinformatics* 29, 15–21. <https://doi.org/10.1093/bioinformatics/bts635>.
- Dvorkin, D., Biehs, B., and Kechris, K. (2013). A graphical model method for integrating multiple sources of genome-scale data. *Stat. Appl. Genet. Mol. Biol.* 12, 469–487. <https://doi.org/10.1515/sagmb-2012-0051>.
- El-Agroudy, N.N., Kurzbach, A., Rodionov, R.N., O'Sullivan, J., Roden, M., Birkenfeld, A.L., and Pesta, D.H. (2019). Are lifestyle therapies effective for NAFLD treatment? *Trends Endocrinol. Metab.* 30, 701–709. <https://doi.org/10.1016/j.tem.2019.07.013>.
- Eslam, M., Sanyal, A.J., and George, J.; International Consensus Panel (2020). MAFLD: A consensus-driven proposed nomenclature for metabolic associated fatty liver disease. *Gastroenterology* 158, 1999–2014.e1. <https://doi.org/10.1053/j.gastro.2019.11.312>.
- Febbraio, M.A., Reibe, S., Shalapour, S., Ooi, G.J., Watt, M.J., and Karin, M. (2019). Preclinical models for studying NASH-driven HCC: how useful are they? *Cell Metab* 29, 18–26. <https://doi.org/10.1016/j.cmet.2018.10.012>.
- Ferlay, J., Soerjomataram, I., Dikshit, R., Eser, S., Mathers, C., Rebelo, M., Parkin, D.M., Forman, D., and Bray, F. (2015). Cancer incidence and mortality worldwide: sources, methods and major patterns in GLOBOCAN 2012. *Int. J. Cancer* 136, E359–E386. <https://doi.org/10.1002/ijc.29210>.
- Friedman, S.L., Neuschwander-Tetri, B.A., Rinella, M., and Sanyal, A.J. (2018). Mechanisms of NAFLD development and therapeutic strategies. *Nat. Med.* 24, 908–922. <https://doi.org/10.1038/s41591-018-0104-9>.
- Hardy, T., Oakley, F., Anstee, Q.M., and Day, C.P. (2016). Nonalcoholic fatty liver disease: pathogenesis and disease spectrum. *Annu. Rev. Pathol.* 11, 451–496. <https://doi.org/10.1146/annurev-pathol-012615-044224>.
- Hu, J.X., Thomas, C.E., and Brunak, S. (2016). Network biology concepts in complex disease comorbidities. *Nat. Rev. Genet.* 17, 615–629. <https://doi.org/10.1038/ng.2016.87>.
- Kim, J.Y., Garcia-Carbonell, R., Yamachika, S., Zhao, P., Dhar, D., Loomba, R., Kaufman, R.J., Saltiel, A.R., and Karin, M. (2018). ER stress drives lipogenesis and steatohepatitis via caspase-2 activation of S1P. *Cell* 175, 133–145.e15. <https://doi.org/10.1016/j.cell.2018.08.020>.
- Langfelder, P. (2020). anRICHment: collections and annotation data for use with anRICHmentMethods. R package. version 1.13-1.
- Langfelder, P., and Horvath, S. (2008). WGCNA: an R package for weighted correlation network analysis. *BMC Bioinformatics* 9, 559. <https://doi.org/10.1186/1471-2105-9-559>.
- Langfelder, P., and Horvath, S. (2012). Fast R functions for robust correlations and hierarchical clustering. *J. Stat. Softw.* 46, i11.
- Langfelder, P., Luo, R., Oldham, M.C., and Horvath, S. (2011). Is my network module preserved and reproducible? *PLoS Comput. Biol.* 7, e1001057. <https://doi.org/10.1371/journal.pcbi.1001057>.
- Langfelder, P., Zhang, B., and Horvath, S. (2008). Defining clusters from a hierarchical cluster tree: the dynamic tree cut package for R. *Bioinformatics* 24, 719–720. <https://doi.org/10.1093/bioinformatics/btm563>.
- Lee, C.Y.D., Daggett, A., Gu, X., Jiang, L.L., Langfelder, P., Li, X., Wang, N., Zhao, Y., Park, C.S., Cooper, Y., et al. (2018). Elevated TREM2 gene dosage reprograms microglia responsiveness and ameliorates pathological phenotypes in Alzheimer's disease models. *Neuron* 97, 1032–1048.e5. <https://doi.org/10.1016/j.neuron.2018.02.002>.
- Lee, T.I., and Young, R.A. (2013). Transcriptional regulation and its misregulation in disease. *Cell* 152, 1237–1251. <https://doi.org/10.1016/j.cell.2013.02.014>.
- Leek, J.T., and Storey, J.D. (2007). Capturing heterogeneity in gene expression studies by surrogate variable analysis. *PLoS Genet* 3, 1724–1735. <https://doi.org/10.1371/journal.pgen.0030161>.

- Li, D., James, B.B., Orsini, L., Pan, Z., Hu, G., and He, S. (2020). MODA: MODA: Module Differential Analysis for weighted gene co-expression network. R package version 1.16.0.
- Lim, Y.W., Chen-Harris, H., Mayba, O., Lianoglou, S., Wuster, A., Bhagale, T., Khan, Z., Mariathasan, S., Daemen, A., Reeder, J., et al. (2018). Germline genetic polymorphisms influence tumor gene expression and immune cell infiltration. *Proc. Natl. Acad. Sci. USA* 115, E11701–E11710. <https://doi.org/10.1073/pnas.1804506115>.
- Love, M.I., Huber, W., and Anders, S. (2014). Moderated estimation of fold change and dispersion for RNA-seq data with DESeq2. *Genome Biol.* 15, 550. <https://doi.org/10.1186/s13059-014-0550-8>.
- Mailman, M.D., Feolo, M., Jin, Y., Kimura, M., Tryka, K., Bagoutdinov, R., Hao, L., Kiang, A., Paschall, J., Phan, L., et al. (2007). The NCBI dbGaP database of genotypes and phenotypes. *Nat. Genet.* 39, 1181–1186. <https://doi.org/10.1038/ng1007-1181>.
- Marengo, A., Rosso, C., and Bugianesi, E. (2016). Liver cancer: connections with obesity, fatty liver, and cirrhosis. *Annu. Rev. Med.* 67, 103–117. <https://doi.org/10.1146/annurev-med-090514-013832>.
- Margolin, A.A., Nemenman, I., Bassi, K., Wiggins, C., Stolovitzky, G., Dalla Favera, R., and Califano, A. (2006). ARACNE: an algorithm for the reconstruction of gene regulatory networks in a mammalian cellular context. *BMC Bioinformatics* 7 (suppl 1), S7. <https://doi.org/10.1186/1471-2105-7-S1-S7>.
- Meyer, P.E., Kontos, K., Lafitte, F., and Bontempi, G. (2007). Information-theoretic inference of large transcriptional regulatory networks. *EURASIP J. Bioinform. Syst. Biol.* 79879. <https://doi.org/10.1155/2007/79879>.
- Meyer, P.E., Lafitte, F., and Bontempi, G. (2008). minet: a R/Bioconductor package for inferring large transcriptional networks using mutual information. *BMC Bioinformatics* 9, 461. <https://doi.org/10.1186/1471-2105-9-461>.
- dbGaP (2019). Accession: phs000178.v11.p8. [https://www.ncbi.nlm.nih.gov/projects/gap/cgi-bin/study.cgi?study\\_id=phs000178.v11.p8](https://www.ncbi.nlm.nih.gov/projects/gap/cgi-bin/study.cgi?study_id=phs000178.v11.p8).
- Nijhout, H.F., Sadre-Marandi, F., Best, J., and Reed, M.C. (2017). Systems biology of phenotypic robustness and plasticity. *Integr. Comp. Biol.* 57, 171–184. <https://doi.org/10.1093/icb/icz076>.
- Nowicka, M., Krieg, C., Crowell, H.L., Weber, L.M., Hartmann, F.J., Guglietta, S., Becher, B., Levesque, M.P., and Robinson, M.D. (2017). CyTOF workflow: differential discovery in high-throughput high-dimensional cytometry datasets. *F1000Res* 6, 748. <https://doi.org/10.12688/f1000research.11622.3>.
- Oldham, M.C., Langfelder, P., and Horvath, S. (2012). Network methods for describing sample relationships in genomic datasets: application to Huntington's disease. *BMC Syst. Biol.* 6, 63. <https://doi.org/10.1186/1752-0509-6-63>.
- Pohlert, T. (2019). PMCMRplus: calculate pairwise multiple comparisons of mean rank sums extended. version 1.4.2. <https://cran.r-project.org/package=PMCMRplus>.
- Quach, H., Rotival, M., Pothlichet, J., Loh, Y.E., Dannemann, M., Zidane, N., Laval, G., Patin, E., Harmant, C., Lopez, M., et al. (2016). Genetic adaptation and neandertal admixture shaped the immune system of human populations. *Cell* 167, 643–656.e17. <https://doi.org/10.1016/j.cell.2016.09.024>.
- R Core Team (2020). R: a language and environment for statistical computing (R Foundation for Statistical Computing). <https://www.R-project.org/>.
- Ritchie, M.E., Phipson, B., Wu, D., Hu, Y., Law, C.W., Shi, W., and Smyth, G.K. (2015). limma powers differential expression analyses for RNA-sequencing and microarray studies. *Nucleic Acids Res* 43, e47. <https://doi.org/10.1093/nar/gkv007>.
- Rohart, F., Gautier, B., Singh, A., and Lê Cao, K.A. (2017). mixOmics: an R package for 'omics feature selection and multiple data integration. *PLoS Comput. Biol.* 13, e1005752. <https://doi.org/10.1371/journal.pcbi.1005752>.
- Shabalin, A.A. (2012). Matrix eQTL: ultra fast eQTL analysis via large matrix operations. *Bioinformatics* 28, 1353–1358. <https://doi.org/10.1093/bioinformatics/bts163>.
- Shen, J., Wang, W., Wu, J., Feng, B., Chen, W., Wang, M., Tang, J., Wang, F., Cheng, F., Pu, L., et al. (2012). Comparative proteomic profiling of human bile reveals SSP411 as a novel biomarker of cholangiocarcinoma. *PLoS One* 7, e47476. <https://doi.org/10.1371/journal.pone.0047476>.
- Stegle, O., Parts, L., Piipari, M., Winn, J., and Durbin, R. (2012). Using probabilistic estimation of expression residuals (PEER) to obtain increased power and interpretability of gene expression analyses. *Nat. Protoc.* 7, 500–507. <https://doi.org/10.1038/nprot.2011.457>.
- Subramanian, A., Tamayo, P., Mootha, V.K., Mukherjee, S., Ebert, B.L., Gillette, M.A., Paulovich, A., Pomeroy, S.L., Golub, T.R., Lander, E.S., and Mesirov, J.P. (2005). Gene set enrichment analysis: a knowledge-based approach for interpreting genome-wide expression profiles. *Proc. Natl. Acad. Sci. USA* 102, 15545–15550. <https://doi.org/10.1073/pnas.0506580102>.
- Sun, X., Vilar, S., and Tatonetti, N.P. (2013). High-throughput methods for combinatorial drug discovery. *Sci. Transl. Med.* 5, 205rv1. <https://doi.org/10.1126/scitranslmed.3006667>.
- Suppli, M.P., Rigbolt, K.T.G., Veidal, S.S., Heebøll, S., Eriksen, P.L., Demant, M., Bagger, J.I., Nielsen, J.C., Orø, D., Thrane, S.W., et al. (2019). Hepatic transcriptome signatures in patients with varying degrees of nonalcoholic fatty liver disease compared with healthy normal-weight individuals. *Am. J. Physiol. Gastrointest. Liver Physiol.* 316, G462–G472. <https://doi.org/10.1152/ajpgi.00358.2018>.
- Therneau, T. (2019). A package for survival analysis in R. R package version 3.1-8. <https://CRAN.R-project.org/package=survival>.
- Therneau, T.M., and Grambsch, P.M. (2000). *Modelling Survival Data: Extending the Cox Model* (Springer).
- Wilcox, R.R. (2012). *Introduction to Robust Estimation and Hypothesis Testing*, Third Edition (Academic Press).
- Yizhak, K., Aguet, F., Kim, J., Hess, J.M., Kübler, K., Grimsby, J., Frazer, R., Zhang, H., Haradhvala, N.J., Rosebrock, D., et al. (2019). RNA sequence analysis reveals macroscopic somatic clonal expansion across normal tissues. *Science* 364, eaaw0726. <https://doi.org/10.1126/science.aaw0726>.
- Younes, R., and Bugianesi, E. (2018). Should we undertake surveillance for HCC in patients with NAFLD? *J. Hepatol.* 68, 326–334. <https://doi.org/10.1016/j.jhep.2017.10.006>.
- Younossi, Z., Anstee, Q.M., Marietti, M., Hardy, T., Henry, L., Eslam, M., George, J., and Bugianesi, E. (2018). Global burden of NAFLD and NASH: trends, predictions, risk factors and prevention. *Nat. Rev. Gastroenterol. Hepatol.* 15, 11–20. <https://doi.org/10.1038/nrgastro.2017.109>.
- Younossi, Z.M., Otgonsuren, M., Henry, L., Venkatesan, C., Mishra, A., Erario, M., and Hunt, S. (2015). Association of nonalcoholic fatty liver disease (NAFLD) with hepatocellular carcinoma (HCC) in the United States from 2004 to 2009. *Hepatology* 62, 1723–1730. <https://doi.org/10.1002/hep.28123>.
- Zhang, B., and Horvath, S. (2005). A general framework for weighted gene co-expression network analysis. *Stat. Appl. Genet. Mol. Biol.* 4, article17. <https://doi.org/10.2202/1544-6115.1128>.

## STAR★METHODS

### KEY RESOURCES TABLE

REAGENT or RESOURCE	SOURCE	IDENTIFIER
<b>Antibodies</b>		
Hamster monoclonal anti-mouse CD3e (clone 145-2C11)	BD Biosciences	RRID: AB_10562036
Hamster monoclonal anti-mouse CD11c (clone N418)	BioLegend	RRID: AB_2563654
Mouse monoclonal anti-mouse NK1.1 (clone PK136)	BD Biosciences	RRID: AB_2728688
Rat monoclonal anti-mouse CD4 (clone GK1.5)	BD Biosciences	RRID: AB_2738734
Rat monoclonal anti-mouse CD8a (clone 53-6.7)	BioLegend	RRID: AB_11219594
Rat monoclonal anti-mouse CD11b (M1/70)	BioLegend	RRID: AB_312789
Rat monoclonal anti-mouse CD45 (clone 30-F11)	BD Biosciences	RRID: AB_2651134
Rat monoclonal anti-mouse F4/80 (clone BM8)	BioLegend	RRID: AB_893481
Rat monoclonal anti-mouse Ly6C (clone HK1.4)	BioLegend	RRID: AB_2565852
Rat monoclonal anti-mouse Ly6G (1A8)	BioLegend	RRID: AB_10643269
Rat monoclonal anti-mouse MHC-II (clone M5/114.15.2)	BioLegend	RRID: AB_2561397
TruStain fcX™; anti mouse CD16/CD32 (Clone 93)	BioLegend	RRID: AB_1574973
<b>Chemicals, peptides, and recombinant proteins</b>		
collagenase-IV	Sigma	C5138; EC No.3.4.24.3
DNase-I	Roche	Cat# 11284932001; EC NO. 3.1.21.1
10X BD Pharm Lyse™	BD Biosciences	Cat# 555899
Zombie Yellow™ Fixable Viability Kit	BioLegend	Cat# 423103
<b>Critical commercial assays</b>		
Sureselect SS RNA library prep, 96	Agilent	G9691B
Agilent DNA 1000 kit	Agilent Technologies	5067-1504
<b>Deposited data</b>		
RNA_Seq (mice)	This paper	GSE148080
RNA_Seq (human fatty liver )	(Suppli et al., 2019)	GSE126848
WGCNA (mouse liver, human liver, TCGA, ICGC liver cancer)	This paper; GitHub	<a href="https://github.com/plangfelder/Core-liver-homeostatic-networks">https://github.com/plangfelder/Core-liver-homeostatic-networks</a>
Flow cytometry	This paper; Mendeley Data	<a href="https://doi.org/10.17632/sfng2h249n.1">https://doi.org/10.17632/sfng2h249n.1</a>
TCGA gene expression data	Genomic Data Commons	<a href="https://portal.gdc.cancer.gov/legacy-archive/search/">https://portal.gdc.cancer.gov/legacy-archive/search/</a>
The database of Genotypes and Phenotypes (dbGaP)	The Cancer Genome Atlas Research Network	phs000178.v11.p8 <a href="https://www.ncbi.nlm.nih.gov/projects/gap/cgi-bin/study.cgi?study_id=phs000178.v11.p8">https://www.ncbi.nlm.nih.gov/projects/gap/cgi-bin/study.cgi?study_id=phs000178.v11.p8</a>
MGI	The Jackson Laboratory	<a href="http://www.informatics.jax.org/homology.shtml">http://www.informatics.jax.org/homology.shtml</a>
ICGC gene expression data	International Cancer Genome Consortium	<a href="https://dcc.icgc.org/">https://dcc.icgc.org/</a>

(Continued on next page)

**Continued**

REAGENT or RESOURCE	SOURCE	IDENTIFIER
Experimental models: Organisms/strains		
Male C57BL/6 mice	Animal Resources Centre	C57BL/6JArc
Software and algorithms		
anRichment 1.13-1	(Langfelder, 2020)	<a href="https://horvath.genetics.ucla.edu/html/CoexpressionNetwork/GeneAnnotation/">https://horvath.genetics.ucla.edu/html/CoexpressionNetwork/GeneAnnotation/</a>
DESeq2 1.26.0	(Love et al., 2014)	<a href="https://bioconductor.org/packages/DESeq2/">https://bioconductor.org/packages/DESeq2/</a>
Dynamic Tree Cut	(Langfelder et al., 2008)	<a href="https://CRAN.R-project.org/package=dynamicTreeCut">https://CRAN.R-project.org/package=dynamicTreeCut</a>
limma 3.38.3	(Ritchie et al., 2015)	<a href="https://doi.org/10.18129/B9.bioc.limma">https://doi.org/10.18129/B9.bioc.limma</a>
MatrixEQTL 2.3	(Shabalin, 2012)	<a href="http://www.bios.unc.edu/research/genomic_software/Matrix_eQTL/">http://www.bios.unc.edu/research/genomic_software/Matrix_eQTL/</a>
Minet 3.48.0	(Meyer et al., 2008)	<a href="https://doi.org/10.18129/B9.bioc.minet">https://doi.org/10.18129/B9.bioc.minet</a>
MixOmics 6.10.9	(Rohart et al., 2017)	<a href="https://bioconductor.org/packages/mixOmics/">https://bioconductor.org/packages/mixOmics/</a>
MODA 1.16.0	(Li et al., 2020)	<a href="https://doi.org/10.18129/B9.bioc.MODA">https://doi.org/10.18129/B9.bioc.MODA</a>
MSigDB 6.2	(Subramanian et al., 2005)	<a href="https://www.gsea-msigdb.org/gsea/msigdb/">https://www.gsea-msigdb.org/gsea/msigdb/</a>
R 4.0.2	(R Core Team, 2020)	<a href="https://www.r-project.org">https://www.r-project.org</a>
STAR 2.6.1c	(Dobin et al., 2013)	<a href="https://github.com/alexdobin/STAR/releases/tag/2.6.1c">https://github.com/alexdobin/STAR/releases/tag/2.6.1c</a>
Surrogate Variable Analysis (R package sva 3.28.0)	(Leek and Storey, 2007)	<a href="https://bioconductor.org/packages/sva/">https://bioconductor.org/packages/sva/</a>
survival 3.1-8	(Therneau, 2019)	<a href="https://cran.r-project.org/web/packages/survival/index.html">https://cran.r-project.org/web/packages/survival/index.html</a>
WGCNA 1.68	(Langfelder and Horvath, 2008)	<a href="http://horvath.genetics.ucla.edu/html/CoexpressionNetwork/Rpackages/WGCNA/">http://horvath.genetics.ucla.edu/html/CoexpressionNetwork/Rpackages/WGCNA/</a>
<b>Other</b>		
Meat Free Rat and Mouse Diet (Normal Chow)	Specialty Feed	N/A
High Sucrose diet	Specialty Feed	SF09-079
High Sucrose + Cholesterol (2%) diet	Specialty Feed	SF14-158
High Sucrose + Cholesterol (0.2%) diet	Specialty Feed	SF18-001
High Sucrose + Cholesterol (2%) + Cholic acid (0.5%) diet	Specialty Feed	SF09-080
High Sucrose + Cholesterol (0.2%) + Cholic acid (0.5%) diet	Specialty Feed	SF15-056
Meat free Rat and mouse diet + Cholesterol (2%) + Cholic acid (0.5%) diet	Specialty Feed	SF14-007
Meat free Rat and mouse + Cholic acid (0.5%) diet	Specialty Feed	SF11-105

## RESOURCE AVAILABILITY

### Lead contact

Further information and requests for resources should be directed to and will be fulfilled by the lead contact, Jacob George ([jacob.george@sydney.edu.au](mailto:jacob.george@sydney.edu.au)).

### Materials availability

The study did not generate new materials.

## Data and code availability

Mice liver RNA-seq source data have been deposited at NCBI GEO dataset and are publicly available under the accession number: GSE148080. CSV spreadsheets and flow-cytometry source data have been deposited at Mendeley and are publicly available at <https://doi.org/10.17632/sfng2h249n.1>. This paper analyses existing publicly available data. These datasets' accession numbers are provided in the [key resource table](#).

WGNA original codes and survival analysis are publicly available at GitHub (<https://github.com/plangfelder/Core-liver-homeostatic-networks>).

The scripts used to generate the figures related to phenotypic data, and flow cytometry analysis reported in this paper are available at Mendeley repository at <https://doi.org/10.17632/sfng2h249n.1>.

Any additional information required to reproduce this work is available from the Lead Contact.

## EXPERIMENTAL MODEL AND SUBJECT DETAILS

### Mice

All procedures were approved by the Western Sydney Local Health District Animal Ethics Committee and conducted in accordance with Animal Experimentation guidelines of the National Health and Medical Research Council (NHMRC) of Australia. Male C57BL/6 mice were obtained from Animal Resources Centre (Perth, Australia) and used for diet studies. Mice were exposed to a 12-hr light/dark cycle in pathogen free conditions with free access to food and water. Mice were given diets containing 34% Sucrose, with and without 0.2% or 2% cholesterol and 0.5% cholic acid (Specialty Feed Service, Glen Forest, Australia) starting at 8 weeks of age for 8-16 weeks. A separate group of male mice were fed normal chow (NC) (meat free rat and mouse chow; Specialty Feed Service, Glen Forest, Australia). At the time of harvest, mice were anesthetized with i.p. ketamine (100 mg/kg)/xylazine (10 mg/kg) injection after a 4-hr fasting period. Blood was collected by cardiac puncture. Liver was harvested, a small portion was rapidly snap frozen in liquid nitrogen and stored at -80 °C. A thin slice of liver tissue was formalin fixed for histology examination. We used 8 mice per group for 8 weeks in diets used for framework analysis. We used 3-5 mice per group for RNA\_Seq, 3 mice per group for flow-cytometry, and 7-8 mice per group for histology analysis. In experiments on NC and HS\_Chol0.2% diet, we used 8 mice per group in 8 and 16 weeks diet studies with histology analysis.

## METHOD DETAILS

### Histology

Liver tissues were fixed in 10% neutral-buffered formalin for 24 hrs and paraffin-embedded tissue sections were stained with hematoxylin and eosin (H&E). The tissues had undergone whole tissue scanning (Hamamatsu Photonics, NanoZoomer, C9600-02).

### Hepatic non-parenchymal cell isolation and flow cytometry

Mice livers were perfused with PBS to remove circulating leukocytes. The isolated perfused liver was minced and digested in RPMI medium containing collagenase-IV (Sigma; C5138; EC No.3.4.24.3; 3.5 mg/g of the liver) and DNase-I (Roche; EC NO. 3.1.21.1; Cat. 11284932001; 8 µg/ml) at 37 °C for 20 min. The cells were then passed through a 70 µm cell strainer with cold RPMI to remove debris and undigested tissue. Next, cells were centrifuged at 50G for 3 min at 4 °C to sediment the majority of hepatocytes. The supernatant was gently collected and centrifuged again at 1600 rpm for 4 min. The cell pellet was collected and suspended in RBC lysis buffer (made from 10X BD Pharm Lyse™ Cat. 555899) for 10 min at room temperature to lyse the red blood cells. The samples were then washed twice with cold PBS to neutralise the residual RBC lysis buffer and digestion buffer; this was followed by re-suspending the pellet in FACS buffer (PBS supplemented with 5% FCS and 1 mM EDTA). Viability of the isolated immune cells was measured by Trypan blue staining. Zombie Yellow™ Fixable Viability Kit (BioLegend Cat. 423103) was used for the exclusion of dead cells. Prior to antibody staining Fc receptor blockade was performed with the use of TruStain fcX™; anti mouse CD16/CD32 (RIDD: AB\_1574973). Samples were then stained with the following antibodies:

Anti CD45 (RRID: [AB\\_2651134](#)), anti CD4 (RRID: [AB\\_2738734](#)), anti NK1.1 (RIDD: AB\_2728688), anti CD3e (RRID: [AB\\_10562036](#)) and anti MHC-II (RRID: AB\_2561397), anti CD8a (RRID: AB\_11219594), anti Ly6C (RRID: [AB\\_2565852](#)), anti CD11b (RRID: AB\_312789), anti CD11c (RRID: [AB\\_2563654](#)), anti F4/80 (RRID: [AB\\_893481](#)) and anti Ly6G (RRID: AB\_10643269). Flow cytometry analysis was performed on an LSR Fortessa (Becton Dickinson) using the FACSDiva software.

### RNA\_Seq

Total liver RNA was extracted using RNAeasy (Qiagen). RNA purity and integrity were confirmed using an Agilent Bioanalyzer. Libraries were prepared from 100 ng total RNA (Sureselect SS RNA library preparation kit, Agilent) and singled-ended sequencing performed on the Illumina HiSeq 2500 using bar-coded multiplexing and a 50 bp read length, yielding a median of 10.7 M reads per sample. Read alignment and junction finding was accomplished using STAR using the 'quantmode GeneCounts' option and an Ensembl mm10 annotation in GTF format. 3 to 5 biological replicates per group from two independent experiments were used for RNA\_Seq.

## QUANTIFICATION AND STATISTICAL ANALYSIS

### Statistical analysis of phenotypic data

Mice phenotypic data (Figures S1A–S1C) are presented as mean  $\pm$  SD and were visualised using GraphPad prism version 8.4.3. In violin plots, the lines depict mean, and the dotted lines represent SD. The data presented are the pool of two independent experiments. 8 biological replicates (mice) were included. We did not exclude any data. In Figures S2 and S3, we have 1 missing value each in HS\_Chol2%\_CA and Chol2%\_CA groups. We first tested the data for Gaussian distribution using the Shapiro-Wilk test and then tested for heteroscedasticity using Bartlett's test, both calculated using Base R v3.5.3. The R package "PMCMRplus v1.4.2" was used to perform the non-parametric Dwass-Steel-Critchlow-Fligner multiple comparisons of mean rank sums test to generate p values (Pohlert, 2019). The R package "effsize v0.7.6" was used to calculate Cohen's d with Hedge's correction for effect size evaluation. Statistical significance is presented as  $P < 0.05$  (\*),  $P < 0.01$  (\*\*),  $P < 0.001$  (\*\*\*) or  $P < 0.0001$  (\*\*\*\*). Effect size is presented as  $g < 0.2$  (n, negligible),  $0.2 < g \leq 0.5$  (+, small),  $0.5 < g \leq 0.8$  (++, medium),  $g > 0.8$  (+++, large).

### Flow cytometry analysis

Manual gating of cell populations was performed using FlowJo v10.6.1 (BD). The following analyses were conducted in the "R 3.5.3" programming language using the "R Studio v 1.2.5001" integrated development environment. FCS files and associated metadata was read into flowSet format using "FlowCore v3.10". Median fluorescence intensity (MFI) values were Arcsinh transformed with a co-factor of 150 as recommended for flow cytometry data (Nowicka et al., 2017). Cell numbers per sample (representing total live, CD45+ singlets) was plotted using "ggplot2 3.2.1". Arcsinh transformed median fluorescence intensity (MFI) values underwent principal component analysis using "mixOmics 3.10". "Non-redundancy score" determined by performing a PCA using the core function *prcomp* across all markers and ranking based on contribution of variability for each marker and plotted using "ggplot2 3.2.1". The top and bottom lines of the NRS boxplots represents the 75%/25% IQR and the lines are min/max. Pheatmap 1.0.12 was used to generate MFI heatmaps. The data presented are representative of one experiment with 3 biological replicates in each group.

### WGCNA, enrichment, and preservation analysis

#### RNA\_Seq data pre-processing

We retained only genes with at least 1 count per million reads in at least 3 samples in mice, 12 samples in human fatty liver dataset, and 1/4 of the samples in human liver cancer datasets. The rationale is to only include genes that are likely to be expressed in at least 1 diet, or disease (minimum group size is 3 in mice and 12 in human fatty liver).

We use a modified version of the sample network methodology originally described in (Oldham et al., 2012). To quantify inter-sample connectivity, we first transformed the raw counts using variance stabilization (R function *varianceStabilizingTransformation*) and then used Euclidean inter-sample distance based on the scaled profiles of the 8000 genes with highest mean expression. The inter-sample connectivities  $k$  were transformed to Z scores using robust standardization,

$$Z_a = \frac{k_a - \text{median}(k)}{1.4826 \times \text{MAD}(k)}$$

where index  $a$  labels samples, MAD is the median absolute deviation, a robust analog of standard deviation, and the constant 1.4826 ensures asymptotic consistency (approximate equality of MAD and standard deviation for large, normally distributed samples). Finally, samples with  $Z_a < -6$  in mice (1 sample),  $Z_a < -4$  in human fatty liver (4 samples), and  $Z_a < -6$  (1 sample from the LIHC-US data set) were removed (Figure S4).

We used Surrogate Variable Analysis (SVA, R package *sva* (Leek and Storey, 2007)) to calculate latent factors representing unwanted variation. The first of these factors (in mice) and the leading two factors (in human fatty liver) were used in the subsequent analysis.

To make DE testing and WGCNA analysis robust against potential outlier measurements (counts) that may remain even after outlier sample removal, we calculate individual observation weights designed to downweigh potential outliers. The weights are constructed separately for each gene. For the calculation of weights in human datasets, we adjusted the data for gender using standard linear models. First, Tukey bi-square-like weights  $\lambda$  (Wilcox, 2012) are calculated for each (variance-stabilized) observation  $x_a$  (index  $a$  labels samples) as

$$\lambda_a = (1 - u_a^2)^2,$$

where

$$u_a = \min\{1, |x_a - \text{median}(x)| / (9\text{MMAD}(x))\}$$

The median is calculated separately for each gene across all samples. MMAD stands for modified MAD, calculated as follows. For each gene, we first set  $\text{MMAD} = \text{MAD}$ . The following conditions are then checked separately for each gene: (1) 10<sup>th</sup> percentile of the weights  $\lambda$  is at least 0.1 (that is, the proportion of observations with weights  $< 0.1$  is less than 10%) (Langfelder and Horvath, 2012) and (2) for each individual group (diet or disease), 40<sup>th</sup> percentile of the weights  $\lambda$  is at least 0.9 (that is, at least 40% of the observation

have a high coefficient of at least 0.9). If both conditions are met, MMAD = MAD. If either condition is not met, MMAD equals the lowest value for which both conditions are met. The rationale is to exclude outliers but ensure that the number of outliers is not too large either overall or in each diet or disease group. This approach has previously been used in (Lee et al., 2018).

### Transformation of data for WGCNA

While individual gene DE analysis use the raw (integer) counts, WGCNA works best with data whose variance is (at least approximately) independent of the mean. For RNA-seq count data, R package DESeq2 (Love et al., 2014) offers variance stabilizing transformation, which can be thought of as log-transforming normalized data with an offset such that in the resulting data, variance is approximately independent of mean expression.

### Differential expression analysis

DE testing was carried out in R using package DESeq2 (Love et al., 2014) version 1.20.0, with diet (in mice) as a variable of interest and first SV as a covariate. In human fatty liver dataset, disease was the variable of interest and gender and leading 2 SVs as a covariate. We disabled replacement of outlier measurements in DESeq2 (because outliers are suppressed using weights) as well as independent filtering of the results because low-expressed genes were filtered out in the pre-processing step.

In the TCGA dataset, DE testing was carried out in R using packages DESeq2 (Love et al., 2014) version 1.28.1, with specimen type (primary tumour solid tissue vs. normal tissue adjacent to primary tumour) as the variable of interest. Donor age and sex were used as covariates, primarily because initial DE analysis indicated a relatively large number of DE genes for each. We did not use other traits because not all samples have valid values; samples with missing covariates cannot be used in modelling. FDR was calculated independently for each diet, disease, or trait contrasts. Genes with FDR below 0.05 were called significant.

### Concordance of DE between mice and human fatty liver

We evaluated concordance of DE for disease/condition in human fatty liver with DE for various diet contrasts in mouse liver data as follows. We mapped genes between mouse and human Entrez identifiers using vertebrate homology information from MGI, The Jackson Laboratory (<http://www.informatics.jax.org/homology.shtml>, downloaded March 2019). We then correlated the genome-wide correlations of DE Z statistics of mapped genes; the correlation is used as a measure of concordance.

### Enrichment of sets of DE genes

We evaluated enrichment of significantly DE genes in the following collections of literature sets:

1. Gene Ontology (GO);
2. Molecular Signatures Database (MSigDB) version 6.2 (Subramanian et al., 2005);
3. BioSystems gene sets, including KEGG, Reactome, Lipid Pathways and BioCYC;
4. Genomic position gene sets; each set contains genes in a 5 Mb window, with two adjacent windows overlapping by 2.5 Mb;
5. Enrichr (Chen et al., 2013) 2016 ChEA library;
6. Enrichr 2015 ENCODE histone modification library;
7. Enrichr 2015 ENCODE TF ChIP-seq library;
8. Enrichr 2017 mirTarBase library (Chou et al., 2018).
9. Collection of DE genes from analysis of mouse liver data

Down- and up-regulated gene sets were tested separately; we did not test enrichment of combined down- and up-regulated genes. The calculations were carried out using R package anRICHment (<https://horvath.genetics.ucla.edu/html/CoexpressionNetwork/GeneAnnotation/>) that implements standard Fisher exact test and a multiple-testing correction across all query and reference gene sets. The multiple testing correction in mice dataset considers all query and reference sets (e.g., in mice, there are 2 directions  $\times$  15 contrasts = 30 query sets and 38,472 reference gene sets), resulting in a stringent Bonferroni multiple testing correction.

### Weighted gene co-expression network analysis

WGCNA was carried on variance-stabilized data in human liver cancer datasets, variance-stabilized data corrected for the 1<sup>st</sup> surrogate variable (SV) in mice and corrected for the leading 2 surrogate variables (SVs) in human fatty liver data. SVs were identified by Surrogate Variable Analysis (SVA). WGCNA (Langfelder and Horvath, 2008) starts by constructing a Topological Overlap (TO) matrix (Zhang and Horvath, 2005). To this end, we used weighted correlation with individual sample weights determined as described above and the “signed hybrid” network in which negatively correlated genes are considered unconnected. Scale free topology analysis suggests that the resulting networks are approximately scale-free for modest soft-thresholding powers. In mice, at power 7, the mean connectivity drops below 100 and median connectivity below about 30 which are reasonable thresholds; hence, we used the soft thresholding power  $\beta=7$  in the analysis. In human fatty liver, at power 6, the mean connectivity drops below 100 and median connectivity is ~10 which are reasonable values; hence, we used the soft thresholding power  $\beta=6$  in the analysis. Scale free topology analysis in liver cancer datasets suggests that the resulting networks are approximately scale-free for modest soft-thresholding powers. We used the soft thresholding power  $\beta=5$  in the analysis of all 3 liver cancer data sets.

WGCNA uses a topological overlap-based dissimilarity as input to average-linkage hierarchical clustering that results in a dendrogram. Modules are identified as branches in the dendrogram using Dynamic Tree Cut (Langfelder et al., 2008). To improve stability of the found modules, we used random subsets of roughly 2/3rds of the samples in each analysis to create 50 sets of perturbed WGCNA module labels. These are then used as an additional input to Dynamic Tree Cut which uses the perturbed module labels to improve module stability. We used two different settings of Dynamic Tree Cut to produce two sets of module labels, one resulting in larger, more robust modules (called the “main” modules) and the second that produces finer split of those main modules that can be thought of as consisting of 2 or more sub-modules. The numeric and color labels of the main modules were chosen such that, if possible, a liver cancer module that overlaps significantly with a module from the human fatty liver analysis carries the same numeric label and color as the human fatty liver module. After module identification, we analyzed the enrichment of genes in each module in the same reference collections of gene sets that we used for enrichment analysis of DE genes.

Since each module groups together correlated genes, it makes sense to represent each module by a single representative expression profile called module eigengene. The module eigengene is defined as the first singular vector of the standardized module expression matrix; this vector explains most of the variance of the module. Module eigengenes lead to a natural measure of similarity (membership) of all individual genes to all modules. The continuous (“fuzzy”) measure of module membership of gene  $i$  in module  $I$  is defined as

$$kME_i^I = \text{cor}(x_i, E^I)$$

where  $x_i$  is the expression profile of gene  $i$  and  $E^I$  is the eigengene of module  $I$ . This definition is applicable to every individual network (data set). The value of module membership lies between  $-1$  and  $1$ . Higher  $kME$  indicate that the expression profile of gene  $i$  is similar to the summary profile of module  $I$ . Since we use signed networks here, we consider module membership near  $-1$  low. The advantage of using correlation to quantify module membership is that the corresponding statistical significance (p-values) can be easily computed. Genes with highest module membership are called hub genes. Hub genes are centrally located inside the module and represent the expression profiles of the entire module. Some genes may have high continuous module membership in two or more modules and may, in this sense, be considered members of (or intermediate between) several modules.

### Association of modules with diet, fatty liver, or traits

We used linear models to relate the module eigengene to individual diet contrasts, or disease contrasts with first SV factor as a covariate, and also used the F test applied to a model in which eigengene expression is regressed on diet as a factor and, as appropriate, the leading SV(s) as covariate(s) to assess overall significance of association with diet or disease (human fatty liver dataset) for each eigengene. For the liver cancer datasets, the module eigengene were related to individual traits with donor sex and age as covariates (no covariates were used in testing association with sex and age themselves).

### Module preservation between human and mouse data

We mapped genes between mouse and human Entrez identifiers using vertebrate homology information from MGI (<http://www.informatics.jax.org/homology.shtml>, downloaded March 2019). Module preservation calculations (Langfelder et al., 2011) were carried out using the modulePreservation function in WGCNA with 500 permutations for mice and human fatty liver and 200 permutations for TCGA dataset. We calculated preservation statistics of human and mouse sub-modules in the respective complementary data set, with the corresponding sub-modules as test modules, and vice-versa.

Module preservation calculations result in multiple observed and permutation-based significance statistics. Although one should consider all statistics, it is often convenient to summarize them into a single (or just a few) summary measures. One of the useful summary measures is Zsummary, a summary of permutation-based preservation Z statistics.

### Enrichment calculations in PPI pairs from BioGRID and STRING databases

We downloaded lists of protein-protein interaction (PPI) pairs from the BioGRID (version 4.0.189) and STRING (version 11.0) databases. We next restricted the lists to those pairs for which both proteins/genes are among the genes retained for WGCNA in the mouse data. The matching was carried out using Entrez IDs. We then carried out simple hypergeometric enrichment calculations testing the null hypothesis that the frequency of PPI pairs with both members in a given module is not greater than the frequency of at least one member not being a member of the module.

### Network construction using MODA, ARACNE and MRNET

We used the package MODA to carry out hierarchical clustering (hc), Louvain and spectral clustering analyses. For each, we selected soft thresholding power 8. For the hc clustering, we used argument cutmethod = “Density”; for Louvain clustering, we used max-size=2000 and for spectral clustering arguments nn=30 and k=20. For the mutual information-based networks, we used functions in the R package minet to calculate the mutual information matrix (function build.mim with default arguments and then used the calculated mutual information as input to functions aracne and mrnet, both with default arguments. We truncated the ARACNE network adjacency values larger than 2 to 2. We next turned the MRNet and truncated ARACNE similarity matrices into dissimilarities by subtracting them from 1 and used them as input to average-linkage hierarchical clustering. Clusters were identified in the resulting trees using Dynamic Tree Cut with deepSplit=4 and minClusterSize=20. Because both networks resulted in a large number of modules,

modules whose eigengenes were correlated at 0.8 or higher were merged using the WGCNA function mergeCloseModules with argument cutHeight=0.2. Module overlaps were tested using the hypergeometric test.

### Module survival stratification

The analysis proceeded in two phases, unstratified and stratified. In the unstratified phase, survival data were regressed against module eigengene values using a Cox proportional hazard model as implemented in the coxph function of the R survival package ([Therneau and Grambsch, 2000](#)). The score test for this model was used to determine which eigengenes showed a significant enough association with survival to justify further analysis. Modules for which the model had  $p \leq 0.05$  were passed to the stratified phase.

Several types of stratification were tried. The basic strategy was to split the values in each module eigengene (with each element of the eigengene representing a patient/measurement) into either two strata, labeled “high” and “low” for the relative expression values; or three strata, labeled “high”, “low”, and “mid.” More specifically, the stratification methods and numbers of strata were:

- median, 2 strata: measurements greater than the median for the eigengene were “high”, while those less than or equal to the median were “low”.
- quantile, 3 strata: measurements greater than the 2/3 quantile (66.666...th percentile) for the eigengene were “high”, those less than or equal to the 1/3 quantile (33.333...rd percentile) were “low”, and others were “mid”.
- quantile wide, 3 strata: measurements greater than the 3/4 quantile (75th percentile) were “high”, less than or equal to the 1/4 quantile (25th percentile) were “low”, others were “mid”.
- mean, 2 strata: measurements greater than the eigengene mean (effectively always 0) were “high”, less than or equal to the mean were “low”.
- zscore, 3 strata; zscore wide, 3 strata: like the corresponding “quantile” methods, but using quantiles of the normal distribution with mean and standard deviation estimated from the elements of the eigengene.
- mix, 2 strata: measurements were subject to a 2-component normal mixture model ([Dvorkin et al., 2013](#)), then classed as “high” or “low” according to component assignment.
- mix, 3 strata: “high”, “low”, or “mid” according to component assignment in a three-component mixture model.

For each module subject to stratified analysis, the eigengene was stratified in each of the above ways, and a log-rank p-value for survival differences between the strata was calculated.

### Module eigengene quantitative trait loci (Module-eQTL)

The data/analyses presented in the current publication are based on the use of study data downloaded from the dbGaP web site, under phs000178.v11.p8 ([Mailman et al., 2007](#); [dbGaP, 2019](#)). Only SNPs that had sufficient BioMart annotation and at least 10 non-major-allele samples were considered as candidate module eQTLs. Sample genotypes were classified as reference allele homozygous, alternate / reference allele heterozygous, or alternate allele homozygous. WGCNA module eigengenes hcM5.1, hcM17, and hcM38 were tested to find possible explanatory SNPs.

Two analyses, a three-way ANOVA and a linear model, were performed with the MatrixEQTL R package ([Shabalin, 2012](#)). In the ANOVA model, each of the three genotypes described above was considered as a factor to explain eigengene expression. In the linear model, expression was regressed against the number of alternate alleles: 0 for reference allele homozygous, 1 for heterozygous, and 2 for alternate allele homozygous.

**Supplemental information**

**Core liver homeostatic co-expression networks  
are preserved but respond to perturbations  
in an organism- and disease-specific manner**

**Saeed Esmaili, Peter Langfelder, T. Grant Belgard, Daniele Vitale, Mahmoud Karimi Azardaryany, Ghazal Alipour Talesh, Mehdi Ramezani-Moghadam, Vikki Ho, Daniel Dvorkin, Suat Dervish, Brian S. Gloss, Henning Grønbæk, Christopher Liddle, and Jacob George**

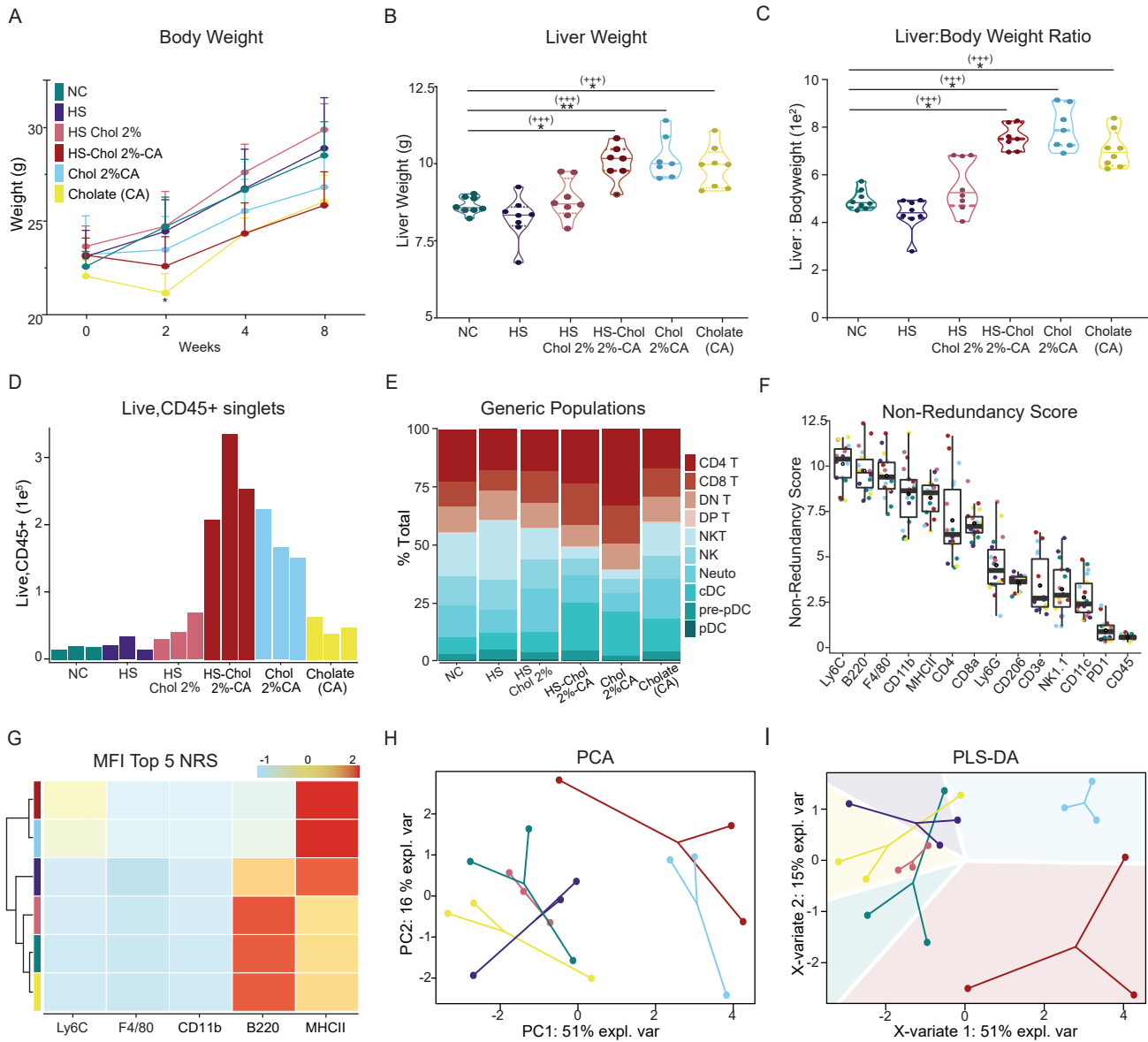


**Figure S1.** Characteristic of mice fed 6 diets, **Related to Figure 1.** **A)** Body weight did not vary significantly across diets. **B-C)** Increase in liverweight and liver:body weight ratio in mice fed the diets containing cholic acid (diets 4, 5, and 6). Data are presented as mean  $\pm$  SD ( $n_{(mice)} = 8$  per group). In violin plots, the lines depict mean, and the dotted lines represent SD. To generate p values and effect size, we used Dwass-Steel-Critchlow-Fligner multiple comparisons of mean rank sums test and Cohen's d with Hedge's correction, respectively. Statistical significance is presented as  $P < 0.05$  (\*), or  $P < 0.01$  (\*\*). Effect size is presented as  $g < 0.2$  (n, negligible),  $0.2 < g \leq 0.5$  (+, small),  $0.5 < g \leq 0.8$  (++, medium),  $g > 0.8$  (+++, large).

**D)** CD45+ Immune cells proliferated greatest in HS\_Chol2%\_CA and Chol2%\_CA. **E)** Stacked percentage bar plot showing manually gated cell populations reveals Ly6G<sup>-</sup> Ly6C<sup>+</sup> cDC population is enriched in HS\_Chol2%\_CA and Chol2%\_CA. **F)** Non-redundancy score (NRS) plot shows “Ly6C”, “B220”, “F4/80”, “CD11b” and “MHCII” as top 5 markers contributing to variability. **G)** Heatmap displaying MFI of the top 5 markers based on NRS reveals variability is concentrated in HS\_Chol2%\_CA and Chol2%\_CA where Ly6C, B220 and MHCII expression has the most impression. **H)** Principal component analysis of marker median mean fluorescence intensity (MFI) shows clustering of HS\_Chol2%\_CA and Chol2%\_CA diets based on variability. **I)** Supervised partial least squares discriminant analysis plot maximally separating distance between diets clearly subdivides the HS\_Chol2%\_CA and Chol2%\_CA diets. ( $n_{(flow cytometry)} = 3$  mice per group).

6 diets: 1) normal chow (NC); 2) high sucrose (HS); 3) high sucrose, cholesterol 2% (HS\_Chol2%); 4) High sucrose, cholesterol and cholic acid (HS\_Chol2%\_CA); 5) High cholesterol and cholic acid (Chol2%\_CA); 6) Cholic acid (CA).

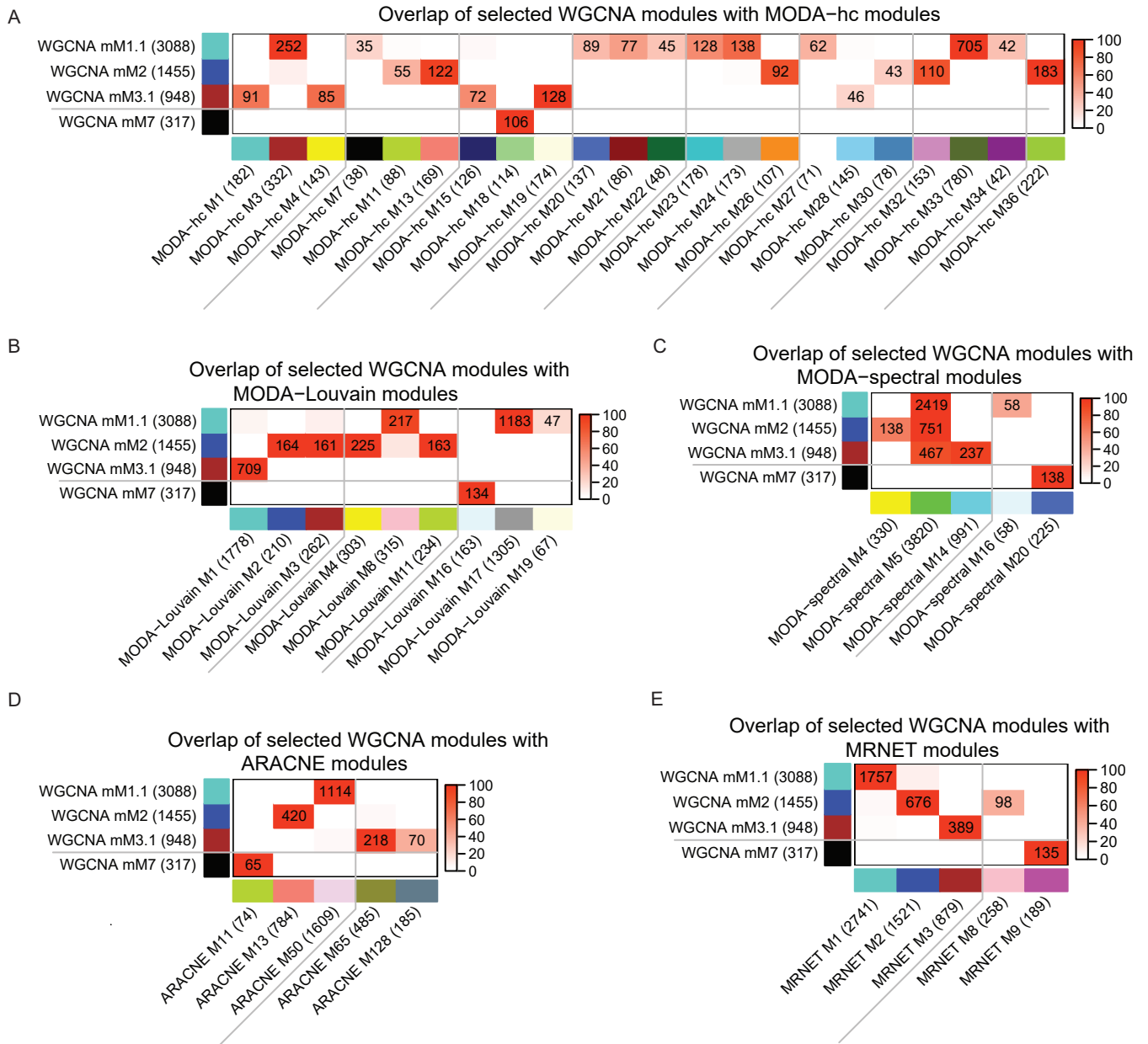


**Figure S2.** WGCNA module recovery by other network analysis methods in the mouse dataset. **Related to STAR Methods** (Network construction using MODA, ARACNE and MRNET). **A)** Overlap of selected WGCNA modules with MODA (hierarchical clustering) modules. **B)** Overlap of selected WGCNA modules with MODA (Louvain clustering) modules. **C)** Overlap of selected WGCNA modules with MODA (Spectral clustering) modules. **D)** Overlap of selected WGCNA modules with ARACNE modules. **E)** Overlap of selected WGCNA modules with MRNET modules.

Heatmap colours represent  $-\log_{10}$  of the hypergeometric enrichment p-value; numbers represent overlap sizes. For easier readability, only overlaps with  $p < 10^{-20}$  have their sizes shown. In row and column labels, numbers in brackets indicate module size.

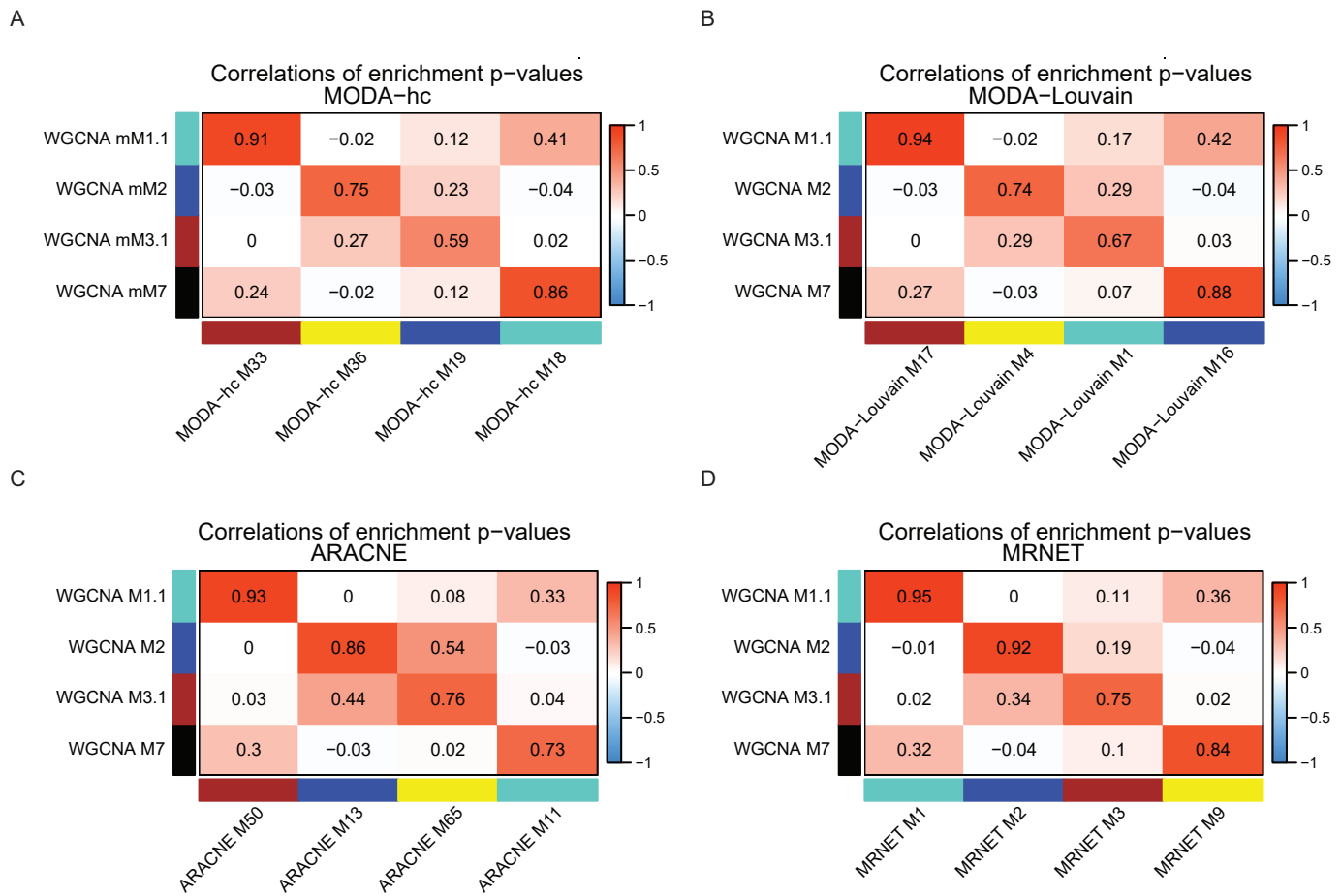
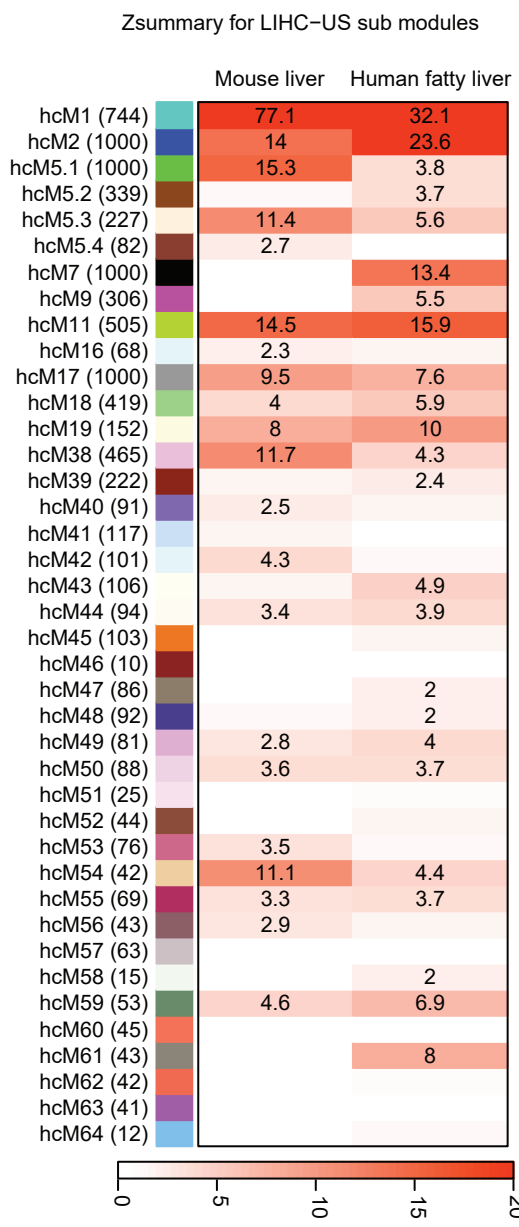
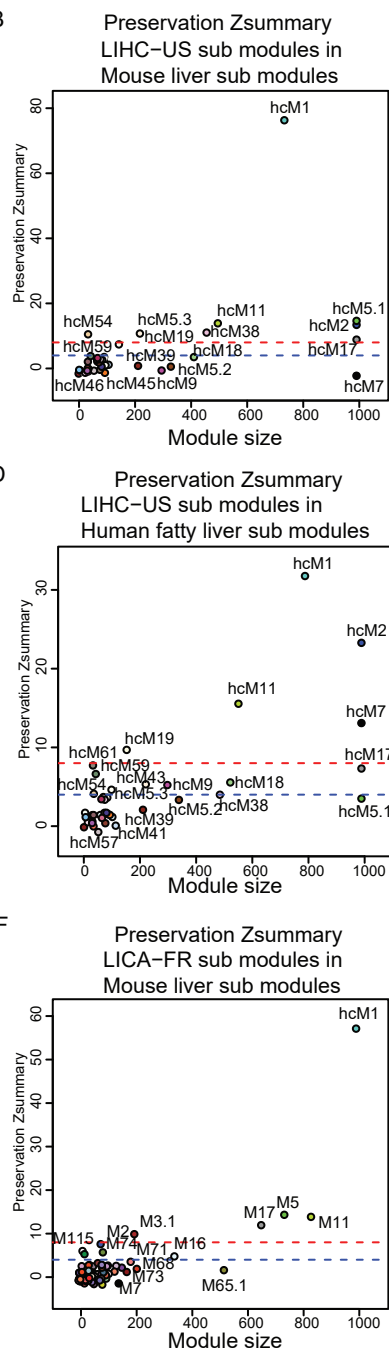


**Figure S3.** Enrichment analysis of MODA, ARACNE, and MRNET modules in the same reference gene sets that were used for enrichment analysis of the WGCNA modules. **Related to STAR Methods** (Network construction using MODA, ARACNE and MRNET). A-D) Correlations of log-transformed enrichment p-values for the 4 selected WGCNA modules (mM1.1, mM2, mM3.1, and mM7) and their closest counterparts in 4 different network analyses (MODA (hierarchical clustering and Louvain clustering), ARACNE, and MRNET). Each cell represents the correlations of log-transformed enrichment p-values across the 38472 reference gene sets used in the enrichment analysis.

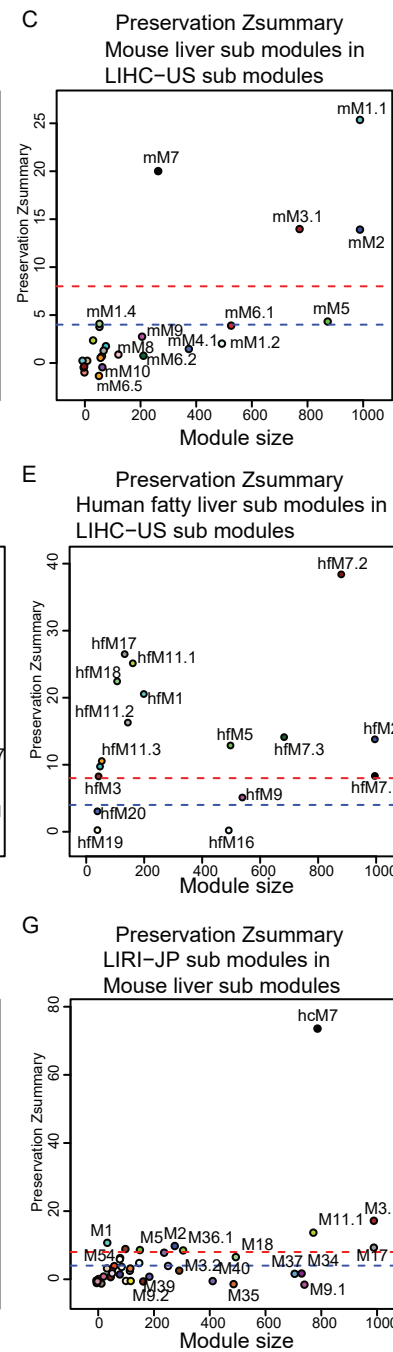
A



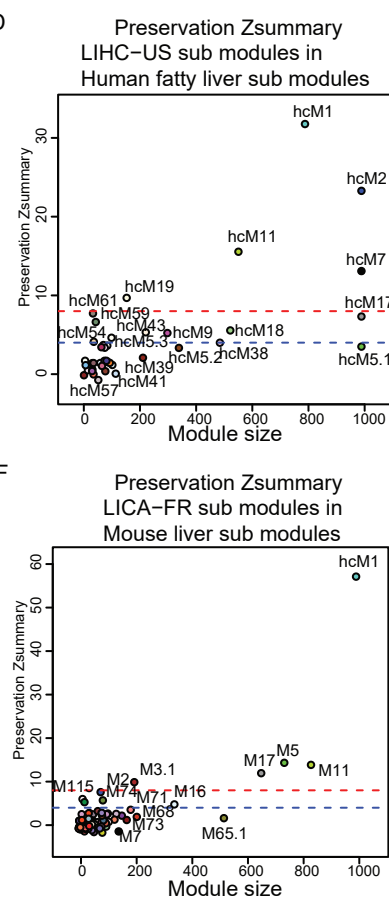
B



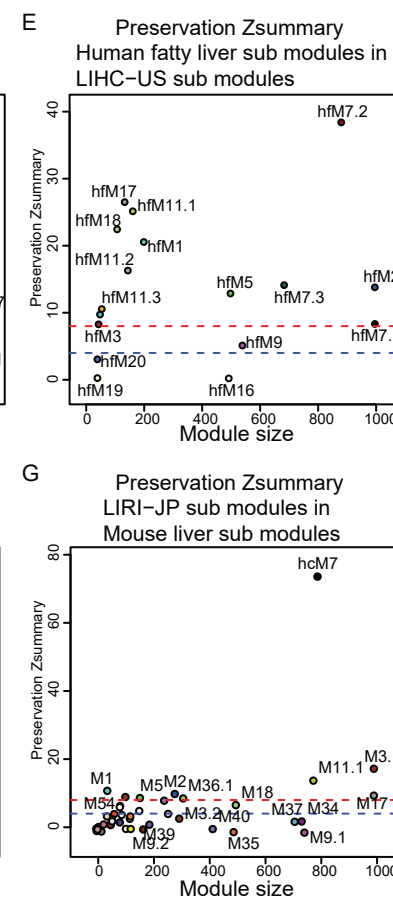
C



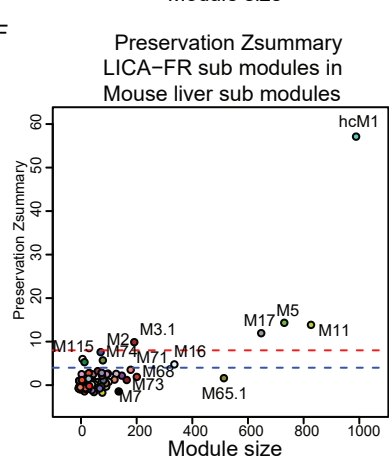
D



E



F



G

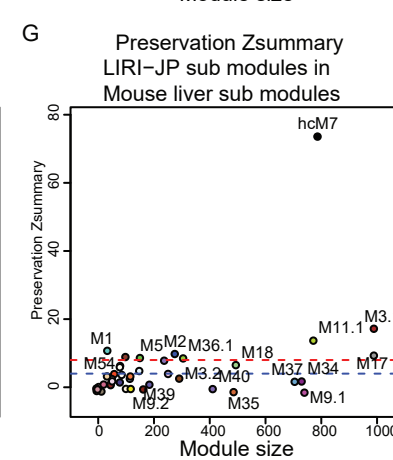


**Figure S4.** Preservation Zsummary of liver cancer sub-modules in mice and human fatty liver sub-modules and the converse module preservation study, [Related to Figure 5](#). **A)** Heatmap representation of module preservation Zsummary statistics of LIHC\_US liver cancer data in mouse and human fatty liver sub-modules. **B)** Preservation Zsummary statistics LIHC\_US sub-modules in mouse sub-modules. **C)** Preservation Zsummary statistics of mouse sub-modules in LIHC\_US sub-modules. **D)** Preservation Zsummary statistics of LIHC\_US sub-modules in human fatty liver sub-modules. **E)** Preservation Zsummary statistics of human fatty liver sub-modules in LIHC\_US sub-modules. **F)** Preservation Zsummary statistics LICA\_FR sub-modules in mouse sub-modules. **G)** Preservation Zsummary statistics LIRI\_JP sub-modules in mouse sub-modules.

Each point represents a module. Point *colour* reflects the module *colour*; where possible, points are also *labelled* by the numeric label of the module. Blue and red lines depict the rough thresholds for moderate ( $Z=4$ ) and strong ( $Z=8$ ) evidence of module preservation.

A

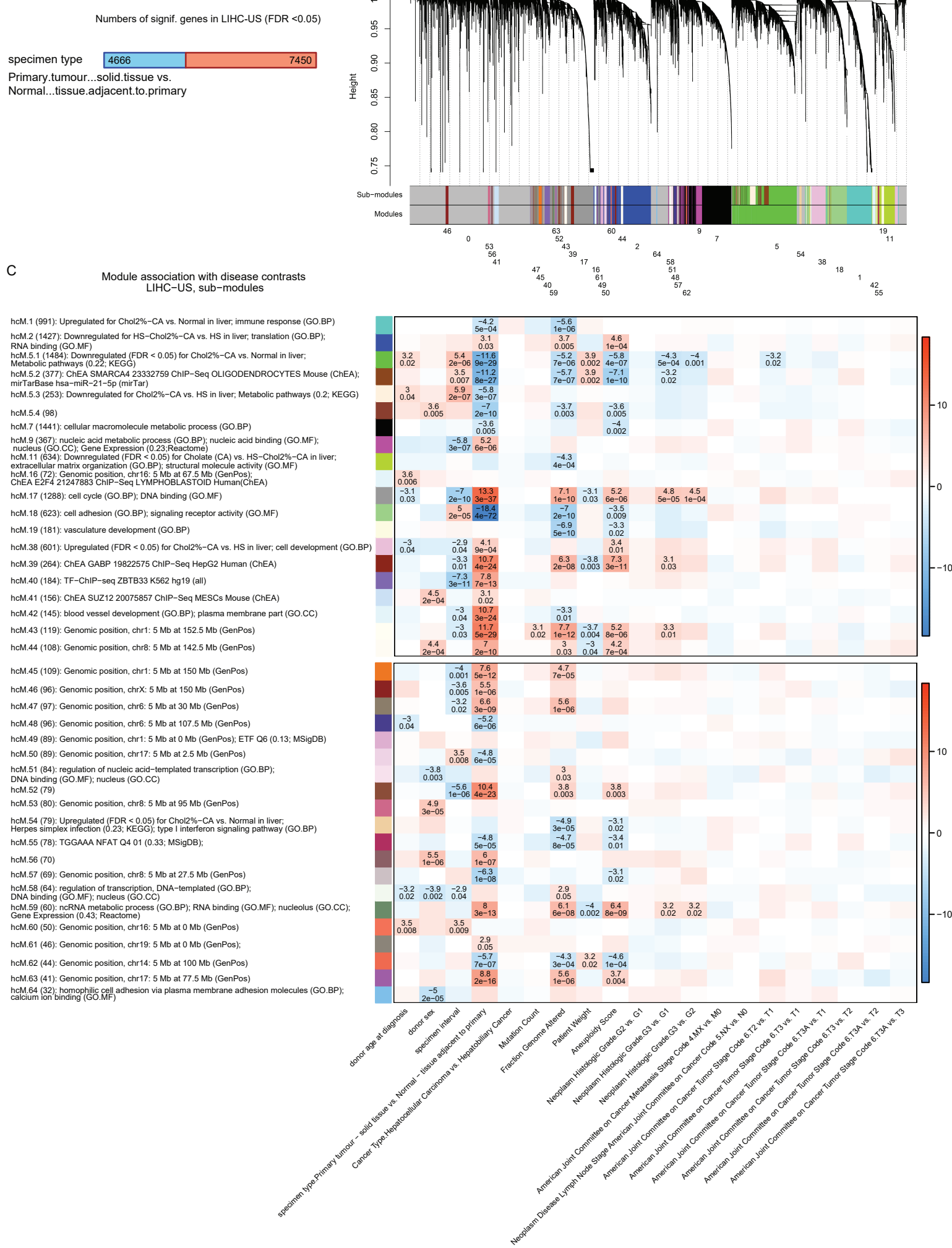


**Figure S5.** Number of differentially expressed genes, gene clustering tree, and association heatmap of module eigengenes with traits in LIHC-US data, **Related to Figure 5.** **A)** Number of significant differentially expressed gene (FDR < 0.05) between tumour and adjacent normal tissues. **B)** Gene clustering tree (dendrogram), module colours and labels in LIHC-US data. Numeric module labels are only shown for main modules. **C)** Association heatmap of module eigengenes of LIHC-US sub-modules with traits. Each row corresponds to a module. Row labels indicate the numeric module label, module size and top enrichment terms. Colour rectangles correspond to the module colour in figure S5B. Each column corresponds to a trait. In the heatmap, numbers give the association significance Z statistic and the FDR estimate. For clarity, Z and FDR are only shown for those cells where FDR<0.05. Colour indicates strength and direction of the association Z statistic.

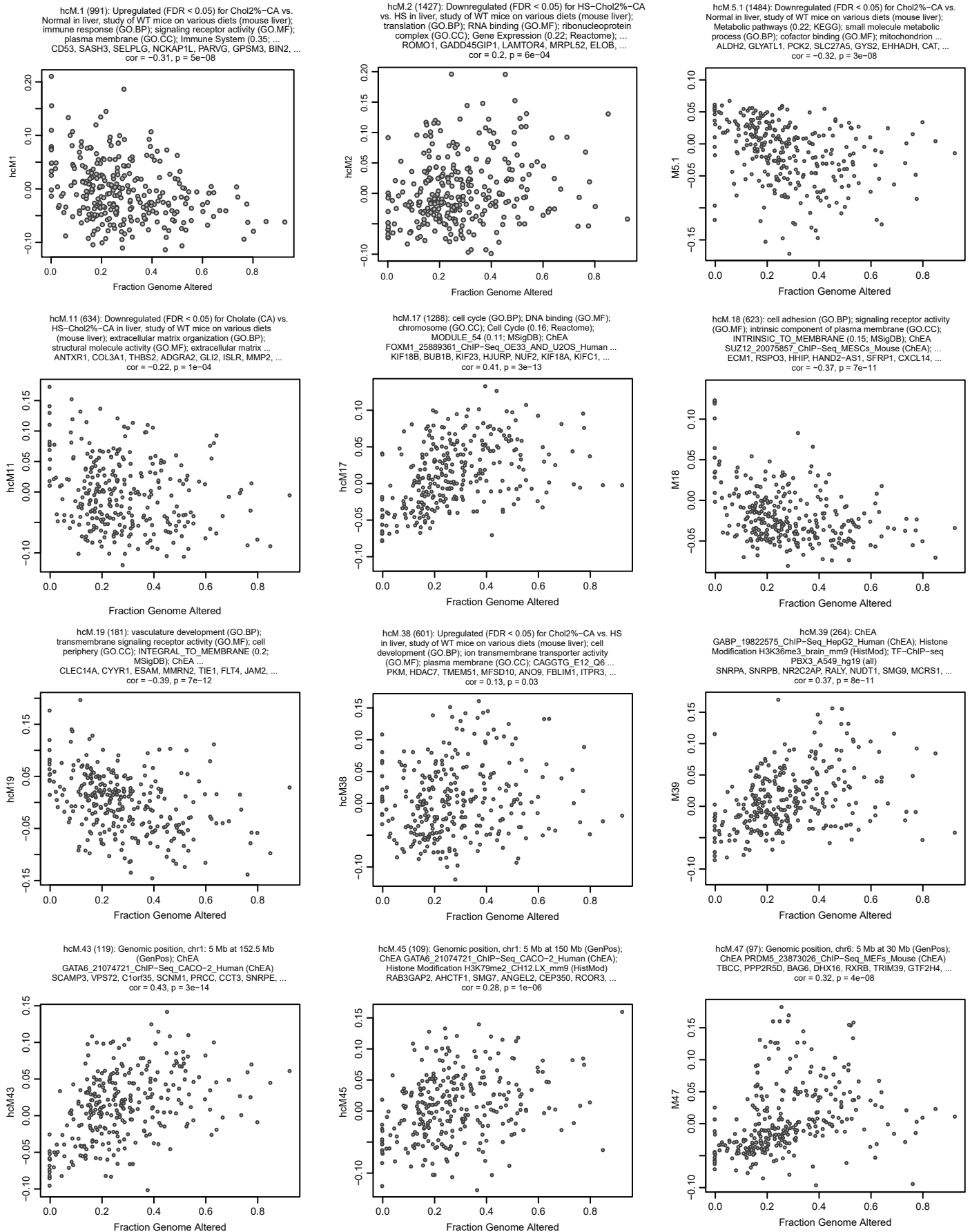


**Figure S6.** Scatterplots of module eigengenes vs. fraction of genome altered in LIHC-US data, **Related to Figure 5**. hcM17 (cell cycle) and hcM43 (Genomic position, Chr:5Mb at 152.5 Mb (GenPos)) are the two modules with strongest association with the fraction of genome altered. Each point represents a sample, n = 291 (288 primary tumours and 3 recurrent tumours).

A

Log-rank p-values for submodules subject to stratified analysis

module	median 2	quantile 3	qu.wide 3	mean 2	zscore 3	zs.wide 3	mix 2	mix 3
hcM5.1	0.03062	0.08963	0.00003	0.08994	0.02104	0.0001	0.09107	0.08795
hcM5.3	0.05608	0.33522	0.26482	0.0473	0.17189	0.07444	0.16395	0.30361
hcM5.4	0.16016	0.28795	0.12035	0.32029	0.09699	0.09413	0.48092	0.51987
hcM17	0.01235	0.00000	0.00000	0.01398	0.00143	0.00000	0.13448	0.00277
hcM19	0.00078	0.07466	0.12588	0.00067	0.05313	0.1265	0.23116	0.24616
hcM38	0.01271	0.01313	0.00476	0.01048	0.00393	0.00543	0.01092	0.01577
hcM41	0.25991	0.59839	0.11897	0.06415	0.22789	0.15443	0.0989	0.25593
hcM46	0.68391	0.24731	0.02498	0.12461	0.05089	0.01806	0.42195	0.08111
hcM49	0.21843	0.3532	0.22844	0.36852	0.42879	0.09982		0.06107
hcM59	0.25319	0.02131	0.00273	0.05647	0.01688	0.00295	0.13911	0.00398

B

module-eQTL\_3way ANOVA

SNP	module	pval	qval
rs2298167	hcM17	6.96E-07	0.000109
rs758097	hcM5.1	4.40E-06	0.000343
rs758097	hcM17	5.12E-05	0.00266
rs2298167	hcM5.1	0.000131	0.005099
rs8076470	hcM17	0.000706	0.021976
rs8053	hcM5.1	0.000845	0.021976
rs8076470	hcM5.1	0.012643	0.155804

C

module-eQTL\_linear

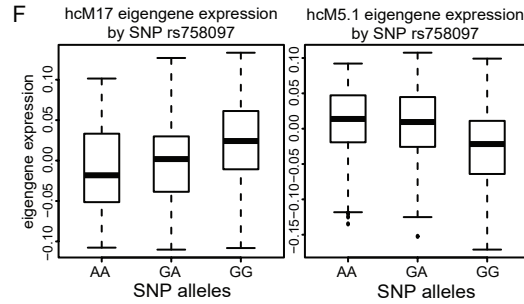
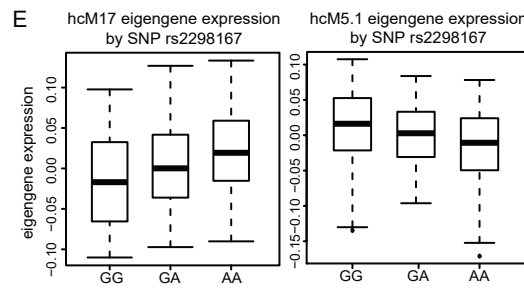
SNP	module	pval	qval	coef	sdcoef	tstat
rs2298167	hcM17	9.99E-08	1.56E-05	0.018185	0.00334	5.444158
rs758097	hcM5.1	1.89E-05	0.001175	-0.01627	0.00375	-4.33841
rs758097	hcM17	2.79E-05	0.001175	0.015997	0.003766	4.247817
rs2298167	hcM5.1	3.01E-05	0.001175	-0.01431	0.003384	-4.22975
rs8076470	hcM17	0.000146	0.004546	-0.01645	0.004281	-3.8418
rs103197	hcM17	0.001203	0.031273	-0.01446	0.004429	-3.26578
rs8076470	hcM5.1	0.003118	0.069481	0.012811	0.004303	2.977189

D

cis-eQTLs based on Lim et al

SNP	symbol	beta	p.value	minor	major	MAF
rs2298167	CGN	-0.74	2.18E-06	A	G	0.3989
rs758097	ZNF419	-0.71	1.72E-07	G	A	0.4031
rs758097	ZNF551	-0.52	2.64E-06	G	A	0.4031
rs8076470	SPATA20	-0.63	9.16E-06	T	C	0.3418
rs103197	DNAJB7	-0.96	4.29E-12	A	G	0.4897

E



F

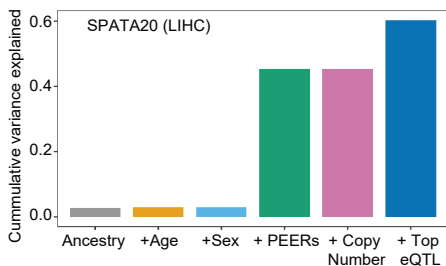


**Figure S7.** Survival analysis based on module expression and subsequent module-eQTL discovery for predictive modules, **Related to Figure 6**. This indicates coordinated gene regulatory mechanisms determine covariance in module expression. **A)** Log-rank p-values for sub-modules subject to stratification analysis. ( $n$  (subjects with available survival and genotype data) = 291) **B)** Module-eQTL using 3-way Anova. **C)** Module-eQTL based on linear model. **D)** SNPs in cis-eQTL based on Lim et. al. **E)** hcM5.1 and hcM17 module expression based on *CGN* alleles. **F)** hcM5.1 and hcM17 expression based on rs758097 SNPs. **G)** The cumulative variance explained for *SPATA20* expression, which shows that there is hardly any influence of ancestry, age, or sex, but a large impact of the top eQTL and a large influence of PEER factors.

Module	Module size	BioGRID p-value	BioGRID enrichment ratio	STRING p-value at threshold 1	STRING enrichment ratio at threshold 1	STRING p-value at threshold 400	STRING enrichment ratio at threshold 400	STRING p-value at threshold 600	STRING enrichment ratio at threshold 600	STRING p-value at threshold 800	STRING enrichment ratio at threshold 800
<b>mM1.1 *</b>	3088	9.74E-51	1.42	<1e-300	2.06	<1e-300	2.57	<1e-300	2.56	<1e-300	2.47
mM1.2	578	6.49E-05	1.61	<1e-300	1.63	4.96E-115	1.68	1.78E-50	1.61	2.15E-18	1.43
mM1.3	74	0.182	2.58	3.25E-48	2.46	1.54E-05	2.03	0.00356	1.92	0.00459	2.13
mM1.4	69	0.000661	7.42	1.71E-29	2.18	1.93E-07	2.39	0.00676	1.91	0.0343	1.84
<b>mM2 *</b>	1455	<1e-300	10.3	<1e-300	3.29	<1e-300	4.71	<1e-300	5.05	<1e-300	4.92
<b>mM3.1 *</b>	948	5.83E-06	1.41	<1e-300	2.42	<1e-300	2.29	<1e-300	2.09	2.76E-247	2.09
mM3.2	93	0.707	0.814	0.104	1.09	0.284	1.11	0.949	0.662	0.747	0.842
mM4.1	1030	1	0.329	1	0.241	1	0.228	1	0.215	1	0.208
mM4.2	42	1	0	1	0.0462	0.992	0.29	0.879	0.548	1	0
mM5	1086	0.0135	1.18	<1e-300	1.52	<1e-300	1.6	1.42E-289	1.81	1.97E-112	1.6
mM6.1	650	1.47E-28	2.72	<1e-300	1.88	1.53E-280	1.99	5.69E-137	1.94	3.90E-92	1.95
mM6.2	258	7.70E-06	2.73	1.42E-187	1.78	1.77E-28	1.75	2.03E-11	1.61	4.80E-06	1.5
mM6.3	100	3.45E-12	11.3	1.25E-189	3.32	5.96E-16	2.52	1.23E-09	2.57	0.00048	2.04
mM6.4	93	0.707	0.814	0.0049	1.18	0.407	1.05	0.107	1.32	0.147	1.35
mM6.5	83	0.0176	4.09	0.002	1.23	0.0618	1.32	0.0951	1.39	0.00848	1.9
mM6.6	80	7.48E-14	16.5	6.39E-37	2.14	2.59E-61	5.77	4.88E-61	8.21	4.87E-60	10.5
<b>mM7 *</b>	317	9.56E-05	2.16	<1e-300	2.41	5.49E-162	2.63	4.68E-37	1.99	0.0618	1.14
mM8	150	5.69E-12	6.86	1.82E-175	2.38	3.87E-29	2.39	8.23E-08	1.86	0.000116	1.74
mM9	244	6.34E-47	9.16	<1e-300	3.23	<1e-300	4.73	1.18E-272	5.53	9.01E-236	6.41
mM10	93	7.06E-07	8.14	2.17E-68	2.38	2.78E-30	3.5	1.82E-25	4.3	7.91E-18	4.38
mM11	52	1	0	4.57E-10	1.83	6.42E-06	2.64	0.00203	2.49	0.167	1.63
mM12	38	1	0	1	0.226	1	0	1	0	1	0
mM13	25	1	0	1	0.265	0.693	0.832	0.363	1.57	1	0
mM14	21	1	0	1	0	1	0	1	0	1	0
mM15	21	1	0	0.994	0.379	1	0	1	0	1	0

\* Core modules

**Table S1.** Enrichment p-values of mouse liver modules in BioGRID and STRING protein-protein interactions (different weight thresholds),

**Related to STAR Methods** (Enrichment calculations in PPI pairs from BioGRID and STRING databases).

WGCNA module	mM 1.1	mM 2	mM3.1	mM 7
Top overlap P in MODA (hc)	<1e-300	2.50E-163	9.63E-127	1.15E-183
Top module in MODA (hc)	33	36	19	18
Eigengene correlation, MODA (hc)	0.994	0.965	0.966	0.977
Top overlap P in MODA (Louvain)	<1e-300	7.05E-183	<1e-300	2.74E-218
Top module in MODA (Louvain)	17	4	1	16
Eigengene correlation, MODA (Louvain)	0.998	0.968	0.991	0.995
Top overlap P in ARACNE	<1e-300	2.16E-263	2.22E-152	6.90E-107
Top module in ARACNE	50	13	65	11
Eigengene correlation, ARACNE	0.998	0.991	0.985	0.978
Top overlap P in MRNET	<1e-300	<1e-300	6.97E-284	1.57E-204
Top module in MRNET	1	2	3	9
Eigengene correlation, MRNET	0.999	0.99	0.972	0.996

**Table S2.** Summary of WGCNA module correspondence with other network analysis methods, **Related to STAR Methods** (Network construction using MODA, ARACNE and MRNET). Summary of module correspondence of 4 selected WGCNA modules (mM1.1, mM2, mM3.1, and mM7) with modules in 4 different network analysis methods (MODA (hierarchical clustering and Louvain clustering), ARACNE, and MRNET). Columns give the overlap p-value of the module with the strongest overlap, the module label and eigengene correlation with the WGCNA module eigengene.